PHYSICAL REVIEW D **86,** 052006 (2012)

Analysis of the resonant components in $\bar{B}_s^0 \to J/\psi\pi^+\pi^-$

R. Aaij *et al.**
(LHCb Collaboration)

(Received 25 April 2012; published 17 September 2012)

The decay $\bar{B}_s^0 \to J/\psi\pi^+\pi^-$ can be exploited to study CP violation. A detailed understanding of its structure is imperative in order to optimize its usefulness. An analysis of this three-body final state is performed using a 1.0 fb^{-1} sample of data produced in 7 TeV pp collisions at the LHC and collected by the LHCb experiment. A modified Dalitz plot analysis of the final state is performed using both the invariant mass spectra and the decay angular distributions. The $\pi^+\pi^-$ system is shown to be dominantly in an S-wave state, and the CP-odd fraction in this $\bar{B}_s^0$ decay is shown to be greater than 0.977 at 95% confidence level. In addition, we report the first measurement of the $J/\psi\pi^+\pi^-$ branching fraction relative to $J/\psi\phi$ of $(19.79 \pm 0.47 \pm 0.52)\%$.

DOI: 10.1103/PhysRevD.86.052006 PACS numbers: 13.25.Hw, 11.30.Er, 14.40.Nd

I. INTRODUCTION

Measurement of mixing-induced CP violation in $\bar{B}_s^0$ decays is of prime importance in probing physics beyond the Standard Model. Final states that are CP eigenstates with large rates and high detection efficiencies are very useful for such studies. The $\bar{B}_s^0 \to J/\psi f_0(980)$, $f_0(980) \to \pi^+\pi^-$ decay mode, a CP-odd eigenstate, was discovered by the LHCb Collaboration [1] and subsequently confirmed by several experiments [2]. As we use the $J/\psi \to \mu^+\mu^-$ decay, the final state has four charged tracks and has high detection efficiency. LHCb has used this mode to measure the CP violating phase ϕ_s [3], which complements measurements in the $J/\psi\phi$ final state [4,5]. It is possible that a larger $\pi^+\pi^-$ mass range could also be used for such studies. Therefore, to fully exploit the $J/\psi\pi^+\pi^-$ final state for measuring CP violation, it is important to determine its resonant and CP content. The tree-level Feynman diagram for the process is shown in Fig. 1.

In this paper the $J/\psi\pi^+$ and $\pi^+\pi^-$ mass spectra and decay angular distributions are used to study the resonant and nonresonant structures. This differs from a classical "Dalitz plot" analysis [6] because one of the particles in the final state, the J/ψ, has spin-1 and its three decay amplitudes must be considered. We first show that there are no evident structures in the $J/\psi\pi^+$ invariant mass, and then model the $\pi^+\pi^-$ invariant mass with a series of resonant and nonresonant amplitudes. The data are then fitted with the coherent sum of these amplitudes. We report on the resonant structure and the CP content of the final state.

*Full author list given at the end of the article.

II. DATA SAMPLE AND ANALYSIS REQUIREMENTS

The data sample contains 1.0 fb^{-1} of integrated luminosity collected with the LHCb detector [7] using pp collisions at a center-of-mass energy of 7 TeV. The detector is a single-arm forward spectrometer covering the pseudorapidity range $2 < \eta < 5$, designed for the study of particles containing b or c quarks. Components include a high precision tracking system consisting of a silicon-strip vertex detector surrounding the pp interaction region, a large-area silicon-strip detector located upstream of a dipole magnet with a bending power of about 4 Tm, and three stations of silicon-strip detectors and straw drift tubes placed downstream. The combined tracking system has a momentum resolution $\Delta p/p$ that varies from 0.4% at 5 GeV to 0.6% at 100 GeV (we work in units where $c = 1$), and an impact parameter resolution of 20 μm for tracks with large transverse momentum with respect to the proton beam direction. Charged hadrons are identified using two ring-imaging Cherenkov detectors. Photon, electron, and hadron candidates are identified by a calorimeter system consisting of scintillating-pad and preshower detectors, an electromagnetic calorimeter, and a hadronic calorimeter. Muons are identified by a muon system composed of alternating layers of iron and multiwire proportional chambers. The trigger consists of a hardware stage, based on information from the calorimeter and muon systems, followed by a software stage that applies a full event reconstruction.

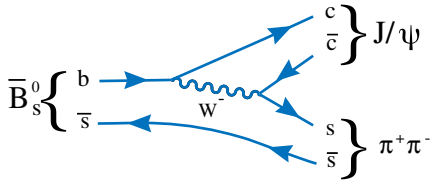

FIG. 1 (color online). Leading order diagram for $\bar{B}_s^0$ decays into $J/\psi\pi^+\pi^-$.

Events selected for this analysis are triggered by a $J/\psi \to \mu^+\mu^-$ decay. Muon candidates are selected at the hardware level using their penetration through iron and detection in a series of tracking chambers. They are also required in the software level to be consistent with coming from the decay of a $\bar{B}_s^0$ meson into a J/ψ. Only J/ψ decays that are triggered on are used.

III. SELECTION REQUIREMENTS

The selection requirements discussed here are imposed to isolate $\bar{B}_s^0$ candidates with high signal yield and minimum background. This is accomplished by first selecting candidate $J/\psi \to \mu^+\mu^-$ decays, selecting a pair of pion candidates of opposite charge and then testing if all four tracks form a common decay vertex. To be considered a $J/\psi \to \mu^+\mu^-$ candidate, particles of opposite charge are required to have transverse momentum, p_{T}, greater than 500 MeV, be identified as muons, and form a vertex with fit χ^2 per number of degrees of freedom (ndf) less than 11. After applying these requirements, there is a large J/ψ signal over a small background [1]. Only candidates with dimuon invariant mass between -48 MeV to $+43$ MeV relative to the observed J/ψ mass peak are selected. The requirement is asymmetric because of final-state electromagnetic radiation. The two muons subsequently are kinematically constrained to the known J/ψ mass [8].

Pion and kaon candidates are positively identified using the ring-imaging Cherenkov system. Cherenkov photons are matched to charged tracks, the emission angles of the photons compared with those expected if the particle is an electron, pion, kaon or proton, and a likelihood is then computed. The particle identification is done by using the logarithm of the likelihood ratio comparing two particle hypotheses (DLL). For pion selection we require $\mathrm{DLL}(\pi - K) > -10$.

Candidate $\pi^+\pi^-$ combinations are selected if each particle is inconsistent with having been produced at the primary vertex. This is done by use of the impact parameter (IP) defined as the minimum distance of approach of the track with respect to the primary vertex. We require that the χ^2 formed by using the hypothesis that the IP is zero be greater than 9 for each track. Furthermore, each pion candidate must have $p_{\mathrm{T}} > 250$ MeV and the scalar sum of the two-pion candidate momentum, $p_{\mathrm{T}}(\pi^+) + p_{\mathrm{T}}(\pi^-)$, must be greater than 900 MeV. To select $\bar{B}_s^0$ candidates we further require that the two pion candidates form a vertex with a $\chi^2 < 10$, that they form a candidate $\bar{B}_s^0$ vertex with the J/ψ where the vertex fit $\chi^2/\mathrm{ndf} < 5$, that this vertex is greater than 1.5 mm from the primary vertex and the angle between the $\bar{B}_s^0$ momentum vector, and the vector from the primary vertex to the $\bar{B}_s^0$ vertex must be less than 11.8 mrad.

We use the decay $\bar{B}_s^0 \to J/\psi\phi$, $\phi \to K^+K^-$ as a normalization and control channel in this paper. The selection criteria are identical to the ones used for $J/\psi\pi^+\pi^-$ except for the particle identification requirement. Kaon candidates are selected requiring that $\mathrm{DLL}(K - \pi) > 0$. Figure 2(a) shows the $J/\psi K^+K^-$ mass for all events with $m(K^+K^-) < 1050$ MeV. The K^+K^- combination is not, however, pure ϕ due to the presence of an S-wave contribution [9]. We determine the ϕ yield by fitting the data to a relativistic P-wave Breit-Wigner function that is convolved with a Gaussian function to account for the experimental mass resolution and a straight line for the S wave. We use the $_s$Plot method to subtract the background [10]. This involves fitting the $J/\psi K^+K^-$ mass spectrum, determining the signal and background weights, and then plotting the resulting weighted mass spectrum, shown in Fig. 2(b). There is a large peak at the ϕ meson mass with a small S-wave component. The mass fit gives $20\,934 \pm 150$ events of which $(95.5 \pm 0.3)\%$ are ϕ and the remainder is the S-wave contribution.

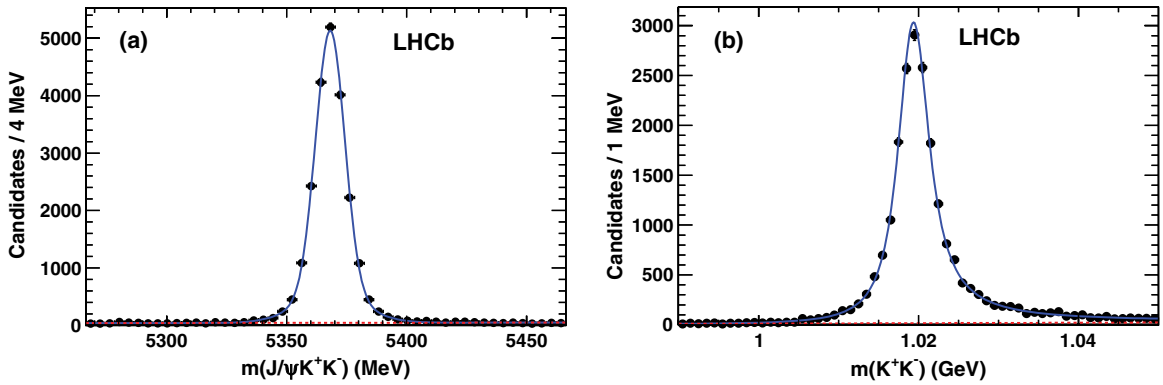

FIG. 2 (color online). (a) Invariant mass spectrum of $J/\psi K^+K^-$ for candidates with $m(K^+K^-) < 1050$ MeV. The data has been fitted with a double-Gaussian signal and linear background functions shown as a dashed line. The solid curve shows the sum. (b) Background subtracted invariant mass spectrum of K^+K^- for events with $m(K^+K^-) < 1050$ MeV. The dashed line (barely visible along the x axis) shows the S-wave contribution and the solid curve is the sum of the S-wave and a P-wave Breit-Wigner functions, fitted to the data.

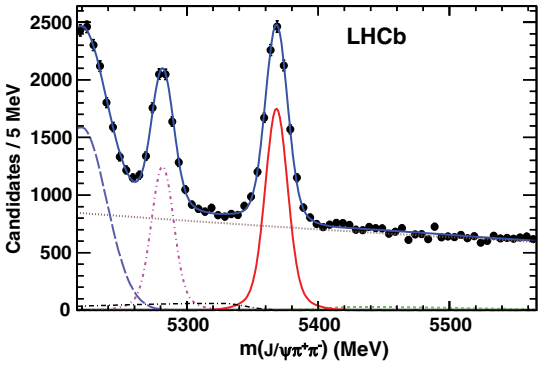

FIG. 3 (color online). Invariant mass of $J/\psi\pi^+\pi^-$ candidate combinations. The data have been fitted with a double-Gaussian signal and several background functions. The (red) solid line shows the $\bar{B}_s^0$ signal, the (brown) dotted line shows the combinatorial background, the (green) short-dashed line shows the B^- background, the (purple) dotted-dashed line is $\bar{B}^0 \to J/\psi\pi^+\pi^-$, the (black) dotted-long-dashed line is the sum of $\bar{B}_s^0 \to J/\psi\eta'$ and $\bar{B}_s^0 \to J/\psi\phi$ when $\phi \to \pi^+\pi^-\pi^0$ backgrounds, the (light blue) long-dashed line is the $\bar{B}^0 \to J/\psi K^-\pi^+$ reflection, and the (blue) solid line is the total.

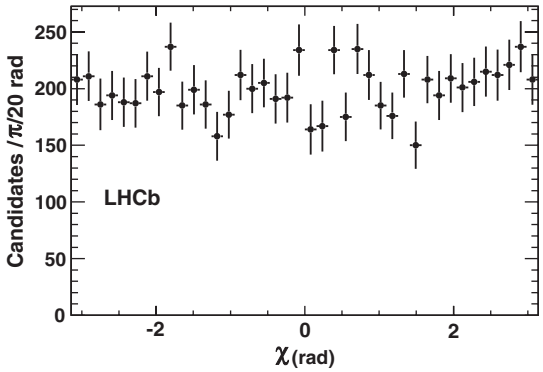

FIG. 4. Background subtracted χ distribution from $\bar{B}_s^0 \to J/\psi\pi^+\pi^-$ candidates.

The invariant mass of the selected $J/\psi\pi^+\pi^-$ combinations, where the dimuon candidate pair is constrained to have the J/ψ mass, is shown in Fig. 3. There is a large peak at the $\bar{B}_s^0$ mass and a smaller one at the $\bar{B}^0$ mass on top of a background. A double-Gaussian function is used to fit the signal, the core Gaussian mean and width are allowed to vary, and the fraction and width ratio for the second Gaussian are fixed to that obtained in the fit of $\bar{B}_s^0 \to J/\psi\phi$. Other components in the fit model take into account contributions from $B^- \to J/\psi K^-(\pi^-)$, $\bar{B}_s^0 \to J/\psi\eta'$, $\eta' \to \rho\gamma$, $\bar{B}_s^0 \to J/\psi\phi$, $\phi \to \pi^+\pi^-\pi^0$, $\bar{B}^0 \to J/\psi\pi^+\pi^-$ backgrounds and a $\bar{B}^0 \to J/\psi K^-\pi^+$ reflection. Here and elsewhere charged conjugated modes are used when appropriate. The shape of the $\bar{B}^0 \to J/\psi\pi^+\pi^-$ signal is taken to be the same as that of the $\bar{B}_s^0$. The exponential combinatorial background shape is taken from wrong-sign combinations, that are the sum of $\pi^+\pi^+$ and $\pi^-\pi^-$ candidates. The shapes of the other components are taken from the Monte Carlo simulation with their normalizations allowed to vary (see Sec. IV B). The mass fit gives 7598 ± 120 signal and 5825 ± 54 background candidates within ± 20 MeV of the $\bar{B}_s^0$ mass peak.

IV. ANALYSIS FORMALISM

The decay of $\bar{B}_s^0 \to J/\psi\pi^+\pi^-$ with the $J/\psi \to \mu^+\mu^-$ can be described by four variables. These are taken to be the invariant mass squared of $J/\psi\pi^+$ ($s_{12} \equiv m^2(J/\psi\pi^+)$), the invariant mass squared of $\pi^+\pi^-$ ($s_{23} \equiv m^2(\pi^+\pi^-)$), the J/ψ helicity angle ($\theta_{J/\psi}$), which is the angle of the μ^+ in the J/ψ rest frame with respect to the J/ψ direction in the $\bar{B}_s^0$ rest frame, and the angle between the J/ψ and $\pi^+\pi^-$ decay planes (χ) in the $\bar{B}_s^0$ rest frame. To improve the resolution of these variables we perform a kinematic fit constraining the $\bar{B}_s^0$ and J/ψ masses to their PDG mass values [8] and recompute the final-state momenta. Because of a limited event sample, we analyze the decay process after integrating over χ. The χ distribution is shown in Fig. 4 after background subtraction using wrong-sign events. The distribution has little structure, and thus the χ acceptance can be integrated over without biasing the other variables.

A. The decay model for $\bar{B}_s^0 \to J/\psi\pi^+\pi^-$

One of the main challenges in performing a Dalitz plot angular analysis is to construct a realistic probability density function (PDF), where both the kinematic and dynamical properties are modeled accurately. The overall PDF given by the sum of signal, S, and background, B, functions is

$$F(s_{12}, s_{23}, \theta_{J/\psi}) = \frac{f_{\rm sig}}{\mathcal{N}_{\rm sig}}\varepsilon(s_{12}, s_{23}, \theta_{J/\psi})S(s_{12}, s_{23}, \theta_{J/\psi}) + \frac{(1 - f_{\rm sig})}{\mathcal{N}_{\rm bkg}}B(s_{12}, s_{23}, \theta_{J/\psi}), \quad (1)$$

where $f_{\rm sig}$ is the fraction of the signal in the fitted region and ε is the detection efficiency. The normalization factors are given by

$$\mathcal{N}_{\rm sig} = \int \varepsilon(s_{12}, s_{23}, \theta_{J/\psi}) \times S(s_{12}, s_{23}, \theta_{J/\psi})ds_{12}ds_{23}d\cos\theta_{J/\psi},$$
$$\mathcal{N}_{\rm bkg} = \int B(s_{12}, s_{23}, \theta_{J/\psi})ds_{12}ds_{23}d\cos\theta_{J/\psi}. \quad (2)$$

In this analysis we apply a formalism similar to that used in Belle's analysis of $\bar{B}^0 \to K^-\pi^+\chi_{c1}$ decays [11].

To investigate if there are visible exotic structures in the $J/\psi\pi^+$ system as claimed in similar decays [12], we examine the $J/\psi\pi^+$ mass distribution shown in Fig. 5. No resonant effects are evident. Examination of the event

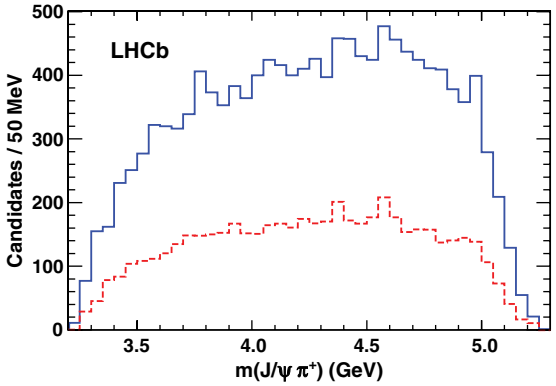

FIG. 5 (color online). Distribution of $m(J/\psi\pi^+)$ for $\bar{B}_s^0 \to J/\psi\pi^+\pi^-$ candidate decays within ± 20 MeV of $\bar{B}_s^0$ mass shown with the (blue) solid line; $m(J/\psi\pi^+)$ for wrong-sign $J/\psi\pi^+\pi^+$ combinations is shown with the (red) dashed line, as an estimate of the background.

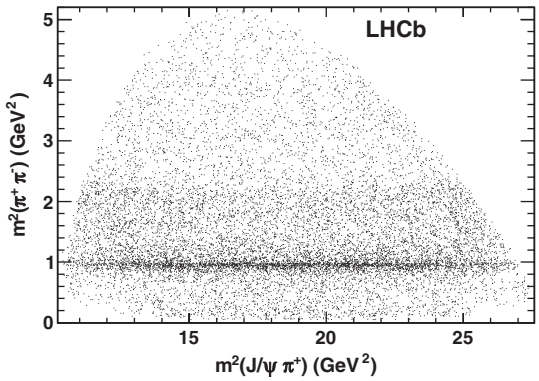

FIG. 6. Distribution of $s_{23} \equiv m^2(\pi^+\pi^-)$ versus $s_{12} \equiv m^2(J/\psi\pi^+)$ for $\bar{B}_s^0$ candidate decays within ± 20 MeV of $\bar{B}_s^0$ mass.

distribution for $m^2(\pi^+\pi^-)$ versus $m^2(J/\psi\pi^+)$ in Fig. 6 shows obvious structure in $m^2(\pi^+\pi^-)$ that we wish to understand.

1. The signal function

The signal function is taken to be the sum over resonant states that can decay into $\pi^+\pi^-$, plus a possible nonresonant S-wave contribution

$$S(s_{12}, s_{23}, \theta_{J/\psi}) = \sum_{\lambda=0,\pm1} \left| \sum_i a_\lambda^{R_i} e^{i\phi_\lambda^{R_i}} \mathcal{A}_\lambda^{R_i}(s_{12}, s_{23}, \theta_{J/\psi}) \right|^2, \quad (3)$$

where $\mathcal{A}_\lambda^{R_i}(s_{12}, s_{23}, \theta_{J/\psi})$ is the amplitude of the decay via an intermediate resonance R_i with helicity λ. Each R_i has an associated amplitude strength $a_\lambda^{R_i}$ for each helicity state λ and a phase $\phi_\lambda^{R_i}$. The amplitudes are defined as

$$\mathcal{A}_\lambda^{R}(s_{12}, s_{23}, \theta_{J/\psi}) = F_B^{(L_B)} A_R(s_{23}) F_R^{(L_R)} T_\lambda \left(\frac{P_B}{m_B}\right)^{L_B} \times \left(\frac{P_R}{\sqrt{s_{23}}}\right)^{L_R} \Theta_\lambda(\theta_{J/\psi}), \quad (4)$$

where P_B is the J/ψ momentum in the $\bar{B}_s^0$ rest frame and P_R is the momentum of either of the two pions in the dipion rest frame, m_B is the $\bar{B}_s^0$ mass, $F_B^{(L_B)}$ and $F_R^{(L_R)}$ are the $\bar{B}_s^0$ meson and R_i resonance decay form factors, L_B is the orbital angular momentum between the J/ψ and $\pi^+\pi^-$ system, and L_R the orbital angular momentum in the $\pi^+\pi^-$ decay, and thus is the same as the spin of the $\pi^+\pi^-$. Since the parent $\bar{B}_s^0$ has spin-0 and the J/ψ is a vector, when the $\pi^+\pi^-$ system forms a spin-0 resonance, $L_B = 1$ and $L_R = 0$. For $\pi^+\pi^-$ resonances with nonzero spin, L_B can be 0, 1, or 2 (1, 2, or 3) for $L_R = 1(2)$ and so on. We take the lowest L_B as the default.

The Blatt-Weisskopf barrier factors $F_B^{(L_B)}$ and $F_R^{(L_R)}$ [13] are

$$F^{(0)} = 1, \qquad F^{(1)} = \frac{\sqrt{1+z_0}}{\sqrt{1+z}}, \qquad F^{(2)} = \frac{\sqrt{z_0^2+3z_0+9}}{\sqrt{z^2+3z+9}}. \quad (5)$$

For the B meson $z = r^2 P_B^2$, where r, the hadron scale, is taken as 5.0 GeV^{-1}; for the R resonance $z = r^2 P_R^2$, and r is taken as 1.5 GeV^{-1}. In both cases $z_0 = r^2 P_0^2$ where P_0 is the decay daughter momentum at the pole mass, different for the $\bar{B}^0$ and the resonance decay.

The angular term, T_λ, is obtained using the helicity formalism and is defined as

$$T_\lambda = d^J_{\lambda 0}(\theta_{\pi\pi}), \quad (6)$$

where d is the Wigner d function [8], J is the resonance spin, and $\theta_{\pi\pi}$ is the $\pi^+\pi^-$ resonance helicity angle, which is defined as the angle of π^+ in the $\pi^+\pi^-$ rest frame with respect to the $\pi^+\pi^-$ direction in the $\bar{B}_s^0$ rest frame and calculated from the other variables as

$$\cos\theta_{\pi\pi} = \frac{[m^2(J/\psi\pi^+) - m^2(J/\psi\pi^-)]m(\pi^+\pi^-)}{4P_R P_B m_B}. \quad (7)$$

The J/ψ helicity-dependent term $\Theta_\lambda(\theta_{J/\psi})$ is defined as

$$\Theta_\lambda(\theta_{J/\psi}) = \sqrt{\sin^2\theta_{J/\psi}} \quad \text{for helicity} = 0,$$
$$\Theta_\lambda(\theta_{J/\psi}) = \sqrt{\frac{1+\cos^2\theta_{J/\psi}}{2}} \quad \text{for helicity} = \pm 1. \quad (8)$$

The function $A_R(s_{23})$ describes the mass squared shape of the resonance R, that in most cases is a Breit-Wigner (BW) amplitude. Complications arise, however, when a new decay channel opens close to the resonant mass. The proximity of a second threshold distorts the line shape of the amplitude. This happens for the $f_0(980)$ because the

K^+K^- decay channel opens. Here we use a Flatté model [14]. For nonresonant processes, the amplitude $A_R(s_{23})$ is constant over the variables s_{12} and s_{23} and has an angular dependence due to the J/ψ decay.

The BW amplitude for a resonance decaying into two spin-0 particles, labeled as 2 and 3, is

$$A_R(s_{23}) = \frac{1}{m_R^2 - s_{23} - im_R\Gamma(s_{23})}, \quad (9)$$

where m_R is the resonance mass, $\Gamma(s_{23})$ is its energy-dependent width that is parametrized as

$$\Gamma(s_{23}) = \Gamma_0\left(\frac{P_R}{P_{R_0}}\right)^{2L_R+1}\left(\frac{m_R}{\sqrt{s_{23}}}\right)F_R^2. \quad (10)$$

Here Γ_0 is the decay width when the invariant mass of the daughter combinations is equal to m_R.

The Flatté model is parametrized as

$$A_R(s_{23}) = \frac{1}{m_R^2 - s_{23} - im_R(g_{\pi\pi}\rho_{\pi\pi} + g_{KK}\rho_{KK})}. \quad (11)$$

The constants $g_{\pi\pi}$ and g_{KK} are the $f_0(980)$ couplings to $\pi^+\pi^-$ and K^+K^- final states, respectively. The ρ factors are given by Lorentz-invariant phase space

$$\rho_{\pi\pi} = \frac{2}{3}\sqrt{1 - \frac{4m_{\pi^\pm}^2}{m^2(\pi^+\pi^-)}} + \frac{1}{3}\sqrt{1 - \frac{4m_{\pi^0}^2}{m^2(\pi^+\pi^-)}}, \quad (12)$$

$$\rho_{KK} = \frac{1}{2}\sqrt{1 - \frac{4m_{K^\pm}^2}{m^2(\pi^+\pi^-)}} + \frac{1}{2}\sqrt{1 - \frac{4m_{K^0}^2}{m^2(\pi^+\pi^-)}}. \quad (13)$$

The nonresonant amplitude is parametrized as

$$\mathcal{A}(s_{12}, s_{23}, \theta_{J/\psi}) = \frac{P_B}{m_B}\sqrt{\sin^2\theta_{J/\psi}}. \quad (14)$$

B. Detection efficiency

The detection efficiency is determined from a sample of 1×10^6 $\bar{B}_s^0 \to J/\psi\pi^+\pi^-$ Monte Carlo (MC) events that are generated flat in phase space with $J/\psi \to \mu^+\mu^-$, using PYTHIA [15] with a special LHCb parameter tune [16], and the LHCb detector simulation based on GEANT4 [17] described in Ref [18]. After the final selections the MC has 78 470 signal events, reflecting an overall efficiency of 7.8%. The acceptance in $\cos\theta_{J/\psi}$ is uniform.

Next we describe the acceptance in terms of the mass squared variables. Both s_{12} and s_{13} range from 10.2 GeV^2 to 27.6 GeV^2, where s_{13} is defined below, and thus are centered at 18.9 GeV^2. We model the detection efficiency using the symmetric Dalitz plot observables

$$x = s_{12} - 18.9\ \text{GeV}^2 \quad \text{and} \quad y = s_{13} - 18.9\ \text{GeV}^2. \quad (15)$$

These variables are related to s_{23} as

$$s_{12} + s_{13} + s_{23} = m_B^2 + m_{J/\psi}^2 + m_{\pi^+}^2 + m_{\pi^-}^2. \quad (16)$$

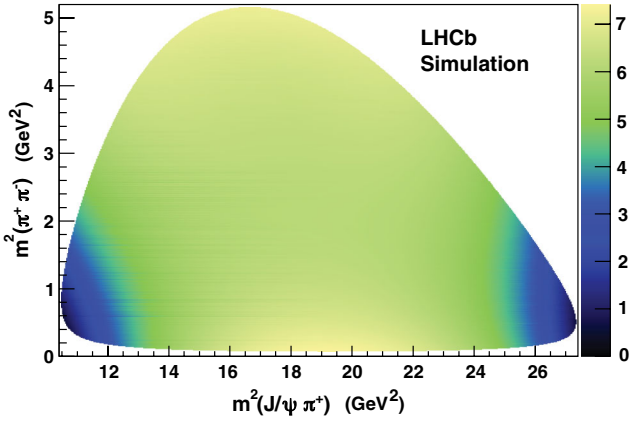

FIG. 7 (color online). Parametrized detection efficiency as a function of $s_{23} \equiv m^2(\pi^+\pi^-)$ versus $s_{12} \equiv m^2(J/\psi\pi^+)$. The scale is arbitrary.

The detection efficiency is parametrized as a symmetric fourth order polynomial function given by

$$\begin{aligned}\varepsilon(s_{12}, s_{23}) = {} & 1 + \varepsilon_1(x+y) + \varepsilon_2(x+y)^2 + \varepsilon_3 xy \\ & + \varepsilon_4(x+y)^3 + \varepsilon_5 xy(x+y) + \varepsilon_6(x+y)^4 \\ & + \varepsilon_7 xy(x+y)^2 + \varepsilon_8 x^2y^2, \end{aligned} \quad (17)$$

where the ε_i are the fit parameters.

The fitted polynomial function is shown in Fig. 7. The projections of the fit used to measure the efficiency parameters are shown in Fig. 8. The efficiency shapes are well described by the parametrization.

To check the detection efficiency we compare our simulated $J/\psi\phi$ events with our measured $J/\psi\phi$ helicity distributions. The events are generated in the same manner as for $J/\psi\pi^+\pi^-$. Here we use the measured helicity amplitudes of $|A_{\|}(0)|^2 = 0.231$ and $|A_0(0)|^2 = 0.524$ [5]. The background subtracted $J/\psi\phi$ angular distributions, $\cos\theta_{J/\psi}$ and $\cos\theta_{KK}$, defined in the same manner as for the $J/\psi\pi^+\pi^-$ decay, are compared in Fig. 9 with the MC simulation. The $\chi^2/\text{ndf} = 389/400$ is determined by binning the angular distributions in two dimensions. The p value is 64.1%. The excellent agreement gives us confidence that the simulation accurately predicts the acceptance.

C. Background composition

The main background source is taken from the wrong-sign combinations within ± 20 MeV of the $\bar{B}_s^0$ mass peak. In addition, an extra 4.5% contribution from combinatorial background formed by J/ψ and random $\rho(770)$, which cannot be present in wrong-sign combinations, is included using a MC sample. The level is determined by measuring the background yield as a function of $\pi^+\pi^-$ mass. The background model is parametrized as

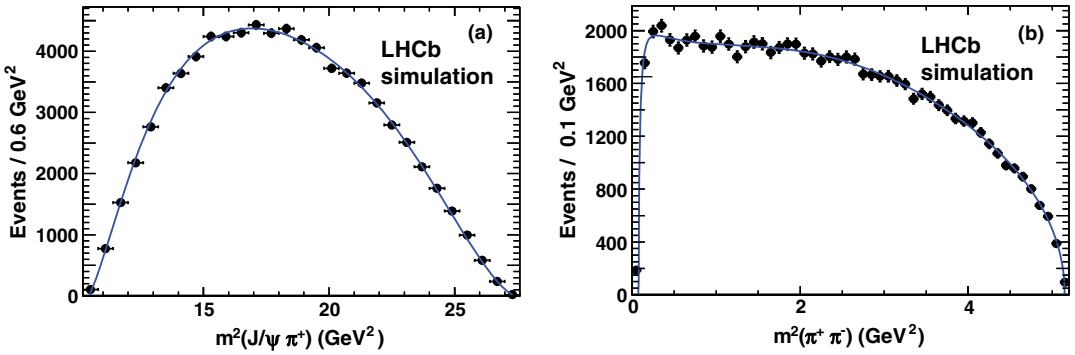

FIG. 8 (color online). Projections of invariant mass squared of (a) $s_{12} \equiv m^2(J/\psi\pi^+)$ and (b) $s_{23} \equiv m^2(\pi^+\pi^-)$ of the MC Dalitz plot used to measure the efficiency parameters. The points represent the MC generated event distributions and the curves the polynomial fit.

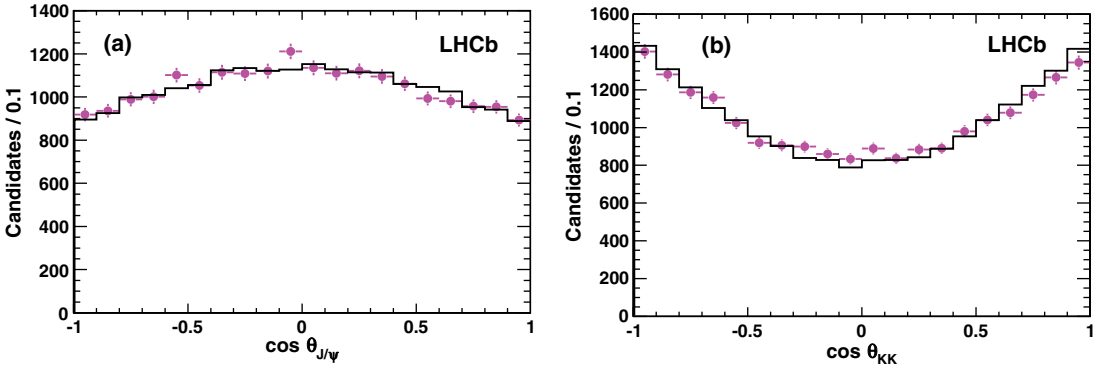

FIG. 9 (color online). Distributions of (a) $\cos\theta_{J/\psi}$, (b) $\cos\theta_{KK}$ for $J/\psi\phi$ background subtracted data (points) compared with the MC simulation (histogram).

$$B(s_{12}, s_{23}, \theta_{J/\psi}) = B_1(s_{12}, s_{23}) \times (1 + \alpha\cos\theta_{J/\psi} + \beta\cos^2\theta_{J/\psi}), \quad (18)$$

where the first part $B_1(s_{12}, s_{23})$ is modeled using the technique of multiquadric radial basis functions [19]. These functions provide a useful way to parametrize multidimensional data giving sensible nonerratic behavior and yet they follow significant variations in a smooth and faithful way. They are useful in this analysis in providing a modeling of the decay angular distributions in the resonance regions. Figure 10 shows the mass squared projections from the fit. The χ^2/ndf of the fit is 182/145. We also used such functions with half the number of parameters and the changes were insignificant. The second part $(1 + \alpha\cos\theta_{J/\psi} + \beta\cos^2\theta_{J/\psi})$ is a function of the J/ψ

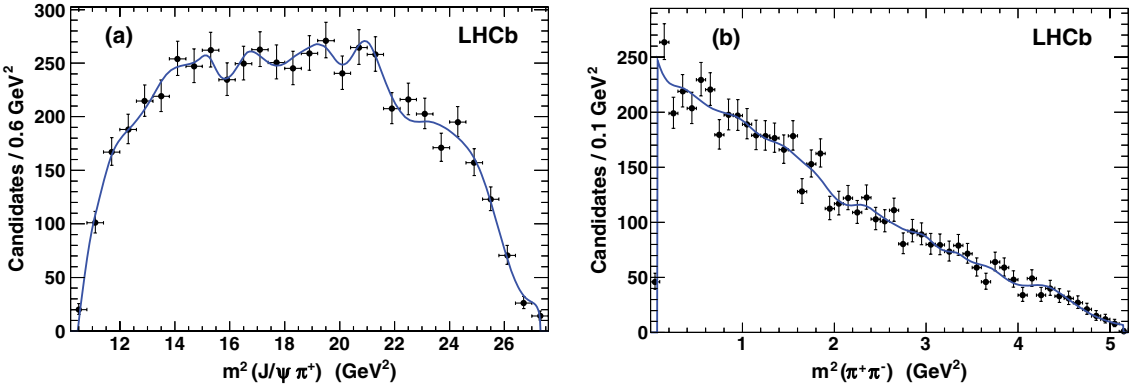

FIG. 10 (color online). Projections of invariant mass squared of (a) $s_{12} \equiv m^2(J/\psi\pi^+)$ and (b) $s_{23} \equiv m^2(\pi^\pm\pi^\pm)$ of the background Dalitz plot.

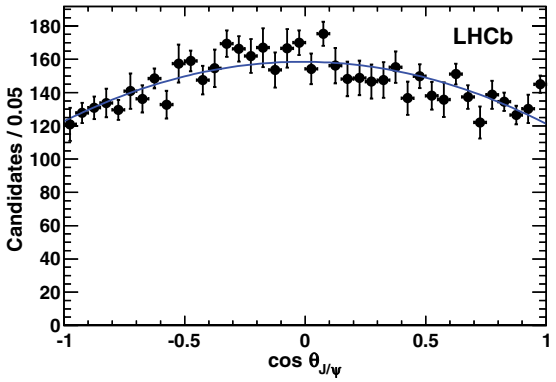

FIG. 11 (color online). The $\cos\theta_{J/\psi}$ distribution of the background and the fitted function $1 + \alpha\cos\theta_{J/\psi} + \beta\cos^2\theta_{J/\psi}$.

helicity angle. The $\cos\theta_{J/\psi}$ distribution of background is shown in Fig. 11, fit with the function $1 + \alpha\cos\theta_{J/\psi} + \beta\cos^2\theta_{J/\psi}$ that determines the parameters $\alpha = -0.0050 \pm 0.0201$ and $\beta = -0.2308 \pm 0.0036$.

V. FINAL-STATE COMPOSITION

A. Resonance models

To study the resonant structures of the decay $\bar{B}_s^0 \to J/\psi\pi^+\pi^-$ we use 13 424 candidates with invariant mass within ± 20 MeV of the $\bar{B}_s^0$ mass peak. This includes both signal and background. Possible resonance candidates in the decay $\bar{B}_s^0 \to J/\psi\pi^+\pi^-$ are listed in Table I. To understand what resonances are likely to contribute, it is important to realize that the $s\bar{s}$ system in Fig. 1 is isoscalar ($I = 0$) so when it produces a single meson it must have zero isospin, resulting in a symmetric isospin wave function for the two-pion system. Since the two pions must be in an overall symmetric state, they must have even total angular momentum. In fact we only need to consider spin-0 and spin-2 particles as there are no known spin-4 particles in the kinematically accessible mass range below 1600 MeV. The particles that could appear are spin-0 $f_0(600)$, spin-0 $f_0(980)$, spin-2 $f_2(1270)$, spin-0 $f_0(1370)$, and spin-0 $f_0(1500)$. Diagrams of higher order than the one shown in Fig. 1 could result in the production of isospin-one $\pi^+\pi^-$ resonances, thus we use the $\rho(770)$ as a test of the presence of these higher order processes.

TABLE I. Possible resonance candidates in the $\bar{B}_s^0 \to J/\psi\pi^+\pi^-$ decay mode.

Resonance	Spin	Helicity	Resonance formalism
$f_0(600)$	0	0	BW
$\rho(770)$	1	0, ± 1	BW
$f_0(980)$	0	0	Flatté
$f_2(1270)$	2	0, ± 1	BW
$f_0(1370)$	0	0	BW
$f_0(1500)$	0	0	BW

We proceed by fitting with a single $f_0(980)$, established from earlier measurements [1], and adding single resonant components until acceptable fits are found. Subsequently, we try the addition of other resonances. The models used are listed in Table II.

The masses and widths of the BW resonances are listed in Table III. When used in the fit they are fixed to these values, except for the $f_0(1370)$, for which they are not well measured, and thus are allowed to vary using their quoted errors as constraints in the fits, taking the errors as being Gaussian.

Besides the mass and width, the Flatté resonance shape has two additional parameters $g_{\pi\pi}$ and g_{KK}, which are also allowed to vary in the fit. Parameters of the nonresonant amplitude are also allowed to vary. One magnitude and one phase in each helicity grouping have to be fixed, since the overall normalization is related to the signal yield, and only relative phases are physically meaningful. The normalization and phase of $f_0(980)$ are fixed to 1 and 0, respectively. The phase of $f_2(1270)$, with helicity $= \pm 1$, is also fixed to zero when it is included. All background and efficiency parameters are held static in the fit.

To determine the complex amplitudes in a specific model, the data are fitted maximizing the unbinned likelihood given as

$$\mathcal{L} = \prod_{i=1}^{N} F(s_{12}^i, s_{23}^i, \theta_{J/\psi}^i), \tag{19}$$

where N is the total number of events, and F is the total PDF defined in Eq. (1). The PDF is constructed from the signal fraction $f_{\rm sig}$, efficiency model $\varepsilon(s_{12}, s_{23})$, background model $B(s_{12}, s_{23}, \theta_{J/\psi})$, and the signal model

TABLE II. Models used in data fit.

Name	Components
Single R	$f_0(980)$
2R	$f_0(980) + f_0(1370)$
3R	$f_0(980) + f_0(1370) + f_2(1270)$
3R + NR	$f_0(980) + f_0(1370) + f_2(1270)$ + nonresonant
3R + NR + $\rho(770)$	$f_0(980) + f_0(1370) + f_2(1270)$ + nonresonant + $\rho(770)$
3R + NR + $f_0(1500)$	$f_0(980) + f_0(1370) + f_2(1270)$ + nonresonant + $f_0(1500)$
3R + NR + $f_0(600)$	$f_0(980) + f_0(1370) + f_2(1270)$ + nonresonant + $f_0(600)$

TABLE III. Breit-Wigner resonance parameters.

Resonance	Mass (MeV)	Width (MeV)	Source
$f_0(600)$	513 ± 32	335 ± 67	CLEO [20]
$\rho(770)$	775.5 ± 0.3	149.1 ± 0.8	PDG [8]
$f_2(1270)$	1275 ± 1	185 ± 3	PDG [8]
$f_0(1370)$	1434 ± 20	172 ± 33	E791 [21]
$f_0(1500)$	1505 ± 6	109 ± 7	PDG [8]

$S(s_{12}, s_{23}, \theta_{J/\psi})$. The PDF needs to be normalized. This is accomplished by first normalizing the J/ψ helicity-dependent part by analytical integration, and then for the mass-dependent part using numerical integration over 500×500 bins.

B. Fit results

In order to compare the different models quantitatively, an estimate of the goodness of fit is calculated from 3D partitions of the one angular and two mass squared variables. We use the Poisson likelihood χ^2 [22] defined as

$$\chi^2 = 2\sum_{i=1}^{N_{\rm bin}}\left[x_i - n_i + n_i \ln\left(\frac{n_i}{x_i}\right)\right], \tag{20}$$

where n_i is the number of events in the three-dimensional bin i and x_i is the expected number of events in that bin according to the fitted likelihood function. A total of $N_{\rm bin} = 1356$ bins are used to calculate the χ^2, using the variables $m^2(J/\psi\pi^+)$, $m^2(\pi^+\pi^-)$, and $\cos\theta_{J/\psi}$. The χ^2/ndf and the negative of the logarithm of the likelihood, $-\ln\mathcal{L}$, of the fits are given in Table IV. There are two solutions of almost equal likelihood for the 3R + NR model. Based on a detailed study of angular distributions (see Sec. V C) we choose one of these solutions and label it as "preferred." The other solution is called "alternate." We will use the differences between these to assign systematic uncertainties to the resonance fractions. The probability is improved noticeably adding components up to 3R + NR. Figure 12 shows the preferred model projections of $m^2(\pi^+\pi^-)$ for the preferred model including only the 3R + NR components. The projections for the other considered models are indiscernible. The preferred model projections of $m^2(J/\psi\pi^+)$ and $\cos\theta_{J/\psi}$ are shown in Fig. 13 for the preferred model 3R + NR fit. The projections of the other preferred model fits including the additional resonances are almost identical.

While a complete description of the decay is given in terms of the fitted amplitudes and phases, knowledge of the contribution of each component can be summarized by defining a fit fraction, $\mathcal{F}_\lambda^R$. To determine $\mathcal{F}_\lambda^R$ we integrate the squared amplitude of R over the Dalitz plot. The yield is then normalized by integrating the entire signal function over the same area. Specifically,

$$\mathcal{F}_\lambda^R = \frac{\int |a_\lambda^R e^{i\phi_\lambda^R}\mathcal{A}_\lambda^R(s_{12}, s_{23}, \theta_{J/\psi})|^2 ds_{12}ds_{23}d\cos\theta_{J/\psi}}{\int S(s_{12}, s_{23}, \theta_{J/\psi})ds_{12}ds_{23}d\cos\theta_{J/\psi}}. \tag{21}$$

Note that the sum of the fit fractions is not necessarily unity due to the potential presence of interference between two resonances. Interference term fractions are given by

$$\mathcal{F}_\lambda^{RR'} = 2\mathcal{R}e\left(\frac{\int a_\lambda^R a_\lambda^{R'} e^{i(\phi_\lambda^R - \phi_\lambda^{R'})}\mathcal{A}_\lambda^R(s_{12}, s_{23}, \theta_{J/\psi})\mathcal{A}_\lambda^{R'*}(s_{12}, s_{23}, \theta_{J/\psi})ds_{12}ds_{23}d\cos\theta_{J/\psi}}{\int S(s_{12}, s_{23}, \theta_{J/\psi})ds_{12}ds_{23}d\cos\theta_{J/\psi}}\right), \tag{22}$$

TABLE IV. χ^2/ndf and $-\ln\mathcal{L}$ of different resonance models.

Resonance model	$-\ln\mathcal{L}$	χ^2/ndf	Probability (%)
Single R	59 269	1956/1352	0
2R	59 001	1498/1348	0.25
3R	58 973	1455/1345	1.88
3R + NR (preferred)	58 945	1415/1343	8.41
3R + NR (alternate)	58 946	1414/1343	8.70
3R + NR + $\rho(770)$ (preferred)	58 945	1418/1341	7.05
3R + NR + $\rho(770)$ (alternate)	58 944	1416/1341	7.57
3R + NR + $f_0(1500)$ (preferred)	58 943	1416/1341	7.57
3R + NR + $f_0(1500)$ (alternate)	58 941	1407/1341	10.26
3R + NR + $f_0(600)$ (preferred)	58 935	1409/1341	9.60
3R + NR + $f_0(600)$ (alternate)	58 937	1412/1341	8.69

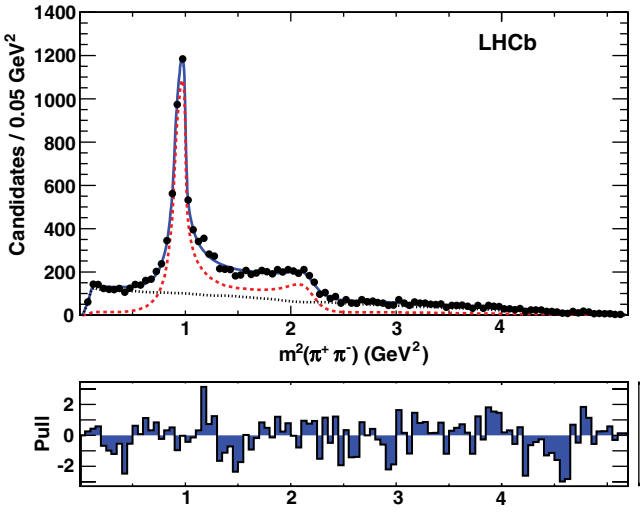

FIG. 12 (color online). Dalitz fit projections of $m^2(\pi^+\pi^-)$ fit with 3R + NR for the preferred model. The points with error bars are data, the signal fit is shown with a (red) dashed line, the background with a (black) dotted line, and the (blue) solid line represents the total. The normalized residuals in each bin are shown below, defined as the difference between the data and the fit divided by the error on the data.

and

$$\sum_{\lambda}\left(\sum_{R}\mathcal{F}_{\lambda}^{R}+\sum_{RR'}\mathcal{F}_{\lambda}^{RR'}\right)=1. \tag{23}$$

If the Dalitz plot has more destructive interference than constructive interference, the total fit fraction will be greater than 1. Note that interference between different spin-J states vanishes because the $d^J_{\lambda 0}$ angular functions in $\mathcal{A}^R_\lambda$ are orthogonal.

The determination of the statistical errors of the fit fractions is difficult because they depend on the statistical errors of every fitted magnitude and phase. A toy Monte Carlo approach is used. We perform 500 toy experiments: each sample is generated according to the model PDF; input parameters are taken from the fit to the data. The correlations of fitted parameters are also taken into account. For each toy experiment the fit fractions are calculated. The distributions of the obtained fit fractions are described by Gaussian functions. The rms widths of the Gaussians are taken as the statistical errors on the corresponding parameters. The fit fractions are listed in Table V.

The 3R + NR fit describes the data well. For models adding more resonances, the additional components never have more than 3 standard deviation (σ) significance, and the fit likelihoods are only slightly improved. In the 3R + NR solution all the components have more than 3σ significance, except for the $f_2(1270)$ where we allow the helicity ± 1 components since the helicity 0 component is significant. In all cases, we find the dominant contribution is S wave, which agrees with our previous less sophisticated analysis [3]. The D-wave contribution is small. The P-wave contribution is consistent with zero, as expected. The fit fractions from the alternate model are listed in Table VI. There are only small changes in the $f_2(1270)$ and $\rho(770)$ components.

The fit fractions of the interference terms for the preferred and alternate models are computed using Eq. (22) and listed in Table VII.

C. Helicity distributions

Only S and D waves contribute to the $\bar{B}_s^0 \to J/\psi\pi^+\pi^-$ final state in the $m(\pi^+\pi^-)$ region below 1550 MeV. Helicity information is already included in the signal model via Eqs. (7) and (8). For a spin-0 $\pi^+\pi^-$ system $\cos\theta_{J/\psi}$ should be distributed as $1-\cos^2\theta_{J/\psi}$ and $\cos\theta_{\pi\pi}$ should be flat. To test our fits we examine the $\cos\theta_{J/\psi}$ and $\cos\theta_{\pi\pi}$ distribution in different regions of $\pi^+\pi^-$ mass. The decay rate with respect to the cosine of the helicity angles is given by [3]

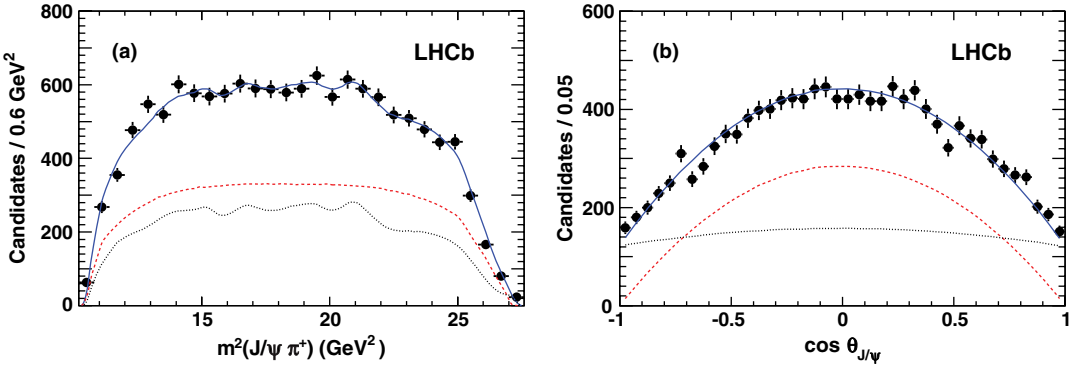

FIG. 13 (color online). Dalitz fit projections of (a) $s_{12} \equiv m^2(J/\psi\pi^+)$ and (b) $\cos\theta_{J/\psi}$ fit with the 3R + NR preferred model. The points with error bars are data; the signal fit is shown with a (red) dashed line, the background with a (black) dotted line, and the (blue) solid line represents the total.

TABLE V. Fit fractions (%) of contributing components for the preferred model. For P and D waves λ represents the final-state helicity. Here ρ refers to the $\rho(770)$ meson.

Components	3R + NR	3R + NR + ρ	3R + NR + $f_0(1500)$	3R + NR + $f_0(600)$
$f_0(980)$	107.1 ± 3.5	104.8 ± 3.9	73.0 ± 5.8	115.2 ± 5.3
$f_0(1370)$	32.6 ± 4.1	32.3 ± 3.7	114 ± 14	34.5 ± 4.0
$f_0(1500)$	···	···	15.0 ± 5.1	···
$f_0(600)$	···	···	···	4.7 ± 2.5
NR	12.84 ± 2.32	12.2 ± 2.2	10.7 ± 2.1	23.7 ± 3.6
$f_2(1270)$, $\lambda = 0$	0.76 ± 0.25	0.77 ± 0.25	1.07 ± 0.37	0.90 ± 0.31
$f_2(1270)$, $\lvert\lambda\rvert = 1$	0.33 ± 1.00	0.26 ± 1.12	1.02 ± 0.83	0.61 ± 0.87
ρ, $\lambda = 0$	···	0.66 ± 0.53	···	···
ρ, $\lvert\lambda\rvert = 1$	···	0.11 ± 0.78	···	···
Sum	153.6 ± 6.0	151.1 ± 6.0	214.4 ± 15.7	179.6 ± 8.0
$-\ln\mathcal{L}$	58945	58944	58943	58935
χ^2/ndf	1415/1343	1418/1341	1416/1341	1409/1341
Probability(%)	8.41	7.05	7.57	9.61

TABLE VI. Fit fractions (%) of contributing components from different models for the alternate solution. For P and D waves λ represents the final-state helicity. Here ρ refers to the $\rho(770)$ meson.

Components	3R + NR	3R + NR + ρ	3R + NR + $f_0(1500)$	3R + NR + $f_0(600)$
$f_0(980)$	100.8 ± 2.9	99.2 ± 4.2	96.9 ± 3.8	111 ± 15
$f_0(1370)$	7.0 ± 0.9	6.9 ± 0.9	3.0 ± 1.7	8.0 ± 1.1
$f_0(1500)$	···	···	4.7 ± 1.7	···
$f_0(600)$	···	···	···	4.3 ± 2.3
NR	13.8 ± 2.3	13.4 ± 2.7	13.4 ± 2.4	24.7 ± 3.9
$f_2(1270)$, $\lambda = 0$	0.51 ± 0.14	0.52 ± 0.14	0.50 ± 0.14	0.51 ± 0.14
$f_2(1270)$, $\lvert\lambda\rvert = 1$	0.24 ± 1.11	0.19 ± 1.38	0.63 ± 0.84	0.48 ± 0.89
ρ, $\lambda = 0$	···	0.43 ± 0.55	···	···
ρ, $\lvert\lambda\rvert = 1$	···	0.14 ± 0.78	···	···
Sum	122.4 ± 4.0	120.8 ± 5.3	119.2 ± 5.2	148.7 ± 15.5
$-\ln\mathcal{L}$	58946	58945	58941	58937
χ^2/ndf	1414/1343	1416/1341	1407/1341	1412/1341
Probability(%)	8.70	7.57	10.26	8.69

$$\frac{d\Gamma}{d\cos\theta_{J/\psi}\, d\cos\theta_{\pi\pi}} = \left| A_{00} + \frac{1}{2} A_{20} e^{i\phi} \sqrt{5}(3\cos^2\theta_{\pi\pi} - 1) \right|^2 \sin^2\theta_{J/\psi} + \frac{1}{4}(|A_{21}|^2 + |A_{2-1}|^2)(15\sin^2\theta_{\pi\pi}\cos^2\theta_{\pi\pi}) \times (1 + \cos^2\theta_{J/\psi}), \quad (24)$$

TABLE VII. Fit fractions (%) of interference terms for both solutions of the 3R + NR model.

Components	Preferred	Alternate
$f_0(980)$ + $f_0(1370)$	−36.6 ± 4.6	−5.4 ± 2.3
$f_0(980)$ + NR	−16.1 ± 2.7	−23.6 ± 2.6
$f_0(1370)$ + NR	0.8 ± 1.0	6.6 ± 0.8
Sum	−53.6 ± 5.5	−22.4 ± 3.6

where A_{00} is the S-wave amplitude, A_{2i}, $i = -1, 0, 1$, the three D-wave amplitudes, and ϕ is the strong phase between A_{00} and A_{20} amplitudes. Nonflat distributions in $\cos\theta_{\pi\pi}$ would indicate interference between the S-wave and D-wave amplitudes.

To investigate the angular structure we then split the helicity distributions into three different $\pi^+\pi^-$ mass regions: one is the $f_0(980)$ region defined within ±90 MeV of the $f_0(980)$ mass and the others are defined within one full width of the $f_2(1270)$ and $f_0(1370)$ masses, respectively (the width values are given in Table III). The $\cos\theta_{J/\psi}$ and $\cos\theta_{\pi\pi}$ background subtracted efficiency corrected distributions for these three different mass regions are presented in Figs. 14 and 15. The distributions are in good agreement with the 3R + NR preferred signal model. Furthermore, splitting into two bins, $[-90, 0]$ and $[0, 90]$ MeV, we see different shapes, because across the pole mass of $f_0(980)$, the $f_0(980)$'s phase changes by π.

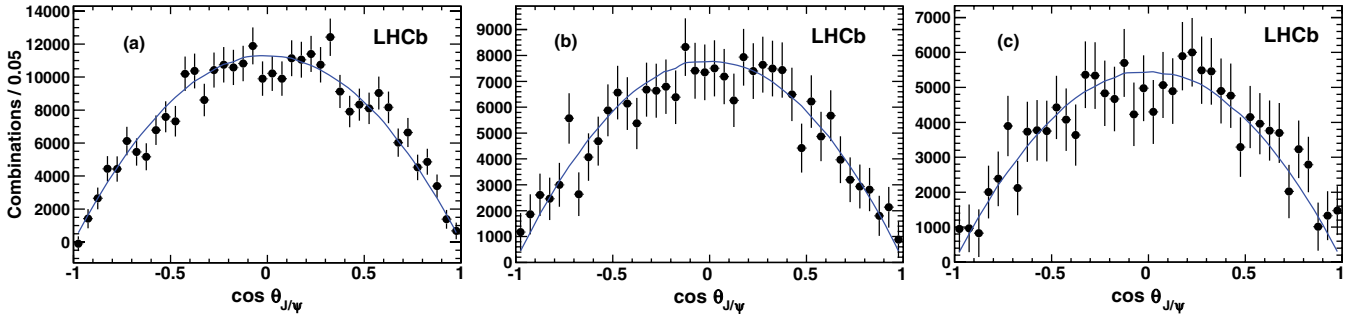

FIG. 14 (color online). Background subtracted and acceptance corrected $\cos\theta_{J/\psi}$ helicity distributions fit with the preferred model: (a) in $f_0(980)$ mass region defined within ± 90 MeV of 980 MeV $\chi^2/\mathrm{ndf} = 39/40$, (b) in $f_2(1270)$ mass region defined within one full width of $f_2(1270)$ mass ($\chi^2/\mathrm{ndf} = 25/40$), (c) in $f_0(1370)$ mass region defined within one full width of $f_2(1370)$ mass ($\chi^2/\mathrm{ndf} = 24/40$). The points with error bars are data and the solid blue lines show the fit from the 3R + NR model.

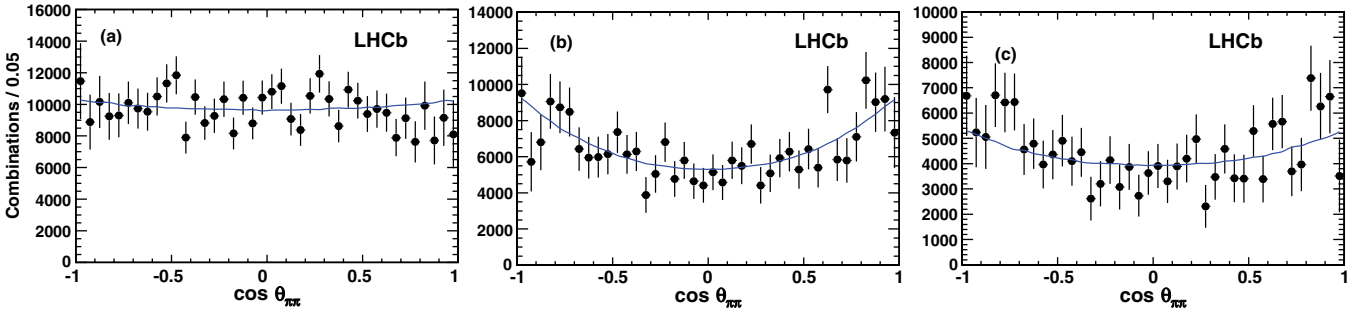

FIG. 15 (color online). Background subtracted and acceptance corrected $\cos\theta_{\pi\pi}$ helicity distributions fit the preferred model: (a) in $f_0(980)$ mass region defined within ± 90 MeV of 980 MeV ($\chi^2/\mathrm{ndf} = 38/40$), (b) in $f_2(1270)$ mass region defined within one full width of $f_2(1270)$ mass ($\chi^2/\mathrm{ndf} = 32/40$), (c) in $f_0(1370)$ mass region defined within one full width of $f_2(1370)$ mass ($\chi^2/\mathrm{ndf} = 37/40$). The points with error bars are data and the solid blue lines show the fit from the 3R + NR model.

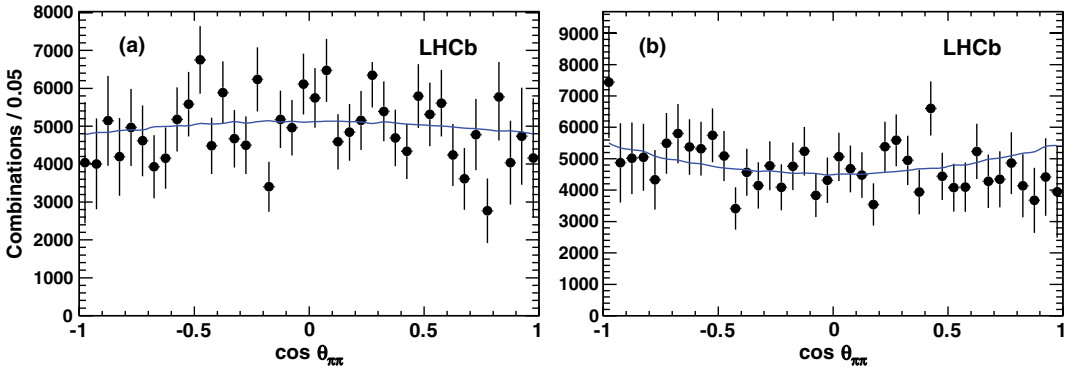

FIG. 16 (color online). Background subtracted and acceptance corrected $\cos\theta_{\pi\pi}$ helicity distributions fit the preferred model: (a) in $[-90, 0]$ MeV of 980 MeV ($\chi^2/\mathrm{ndf} = 41/40$), (b) in $[0, 90]$ MeV of 980 MeV ($\chi^2/\mathrm{ndf} = 31/40$).

Hence the relative phase between $f_0(980)$ and the small D wave in the two regions changes very sharply. This feature is reproduced well by the preferred model and shown in Fig. 16. The "alternate" model gives an acceptable, but poorer, description.

D. Resonance parameters

The fit results from the four-component best fit are listed in Table VIII for both the preferred and alternate solutions. The table summarizes the $f_0(980)$ mass, the Flatté resonances parameters $g_{\pi\pi}$, $g_{KK}/g_{\pi\pi}$, $f_0(1370)$ mass and width, and the phases of the contributing resonances.

The mass and resonance parameters depend strongly on the final state in which they are measured and the form of the resonance fitting function. Thus we do not quote systematic errors on these values. The value found for the $f_0(980)$ mass in the Flatté function 939.9 ± 6.3 MeV is

TABLE VIII. Fit results from the 3R + NR model for both the preferred and alternate solutions. ϕ indicates the phase with respect to the $f_0(980)$. For the $f_2(1270)$, λ represents the final-state helicity.

Parameters	Preferred	Alternate
$m_{f_0(980)}$(MeV)	939.9 ± 6.3	939.2 ± 6.5
$g_{\pi\pi}$(MeV)	199 ± 30	197 ± 25
$g_{KK}/g_{\pi\pi}$	3.0 ± 0.3	3.1 ± 0.2
$m_{f_0(1370)}$(MeV)	1475.1 ± 6.3	1474.4 ± 6.0
$\Gamma_{f_0(1370)}$(MeV)	113 ± 11	108 ± 11
ϕ_{980}	0 (fixed)	0 (fixed)
ϕ_{1370}	241.5 ± 6.3	181.7 ± 8.4
$\phi_{\rm NR}$	217.0 ± 3.7	232.2 ± 3.7
ϕ_{1270}, $\lambda = 0$	165 ± 15	118 ± 15
ϕ_{1270}, $\lvert\lambda\rvert = 1$	0 (fixed)	0 (fixed)

lower than most determinations, although the observed peak value is close to 980 MeV, the estimated PDG value [8]. This is due to the interference from other resonances. The BES Collaboration using the same functional form found a mass value of $965 \pm 8 \pm 6$ MeV in the $J/\psi \to \phi\pi^+\pi^-$ final state [23]. They also found roughly similar values of the coupling constants as ours, $g_{\pi\pi} = 165 \pm 10 \pm 15$ MeV and $g_{KK}/g_{\pi\pi} = 4.21 \pm 0.25 \pm 0.21$. The PDG provides only estimated values for the $f_0(1370)$ mass of 1200–1500 MeV and width 200–500 MeV, respectively [8]. Our result is within both of these ranges.

E. Angular moments

The angular moment distributions provide an additional way of visualizing the effects of different resonances and their interferences, similar to a partial wave analysis. This technique has been used in previous studies [24].

We define the angular moments $\langle Y_l^0\rangle$ as the efficiency corrected and background subtracted $\pi^+\pi^-$ invariant mass distributions, weighted by spherical harmonic functions

$$\langle Y_l^0\rangle = \int_{-1}^{1} d\Gamma(m_{\pi\pi}, \cos\theta_{\pi\pi}) Y_l^0(\cos\theta_{\pi\pi}) d\cos\theta_{\pi\pi}. \quad (25)$$

The spherical harmonic functions satisfy

$$\int_{-1}^{1} Y_i^0(\cos\theta_{\pi\pi}) Y_j^0(\cos\theta_{\pi\pi}) d\cos\theta_{\pi\pi} = \frac{\delta_{ij}}{2\pi}. \quad (26)$$

If we assume that no $\pi^+\pi^-$ partial waves of a higher order than D wave contribute, then we can express the differential decay rate ($d\Gamma$) derived from Eq. (3) in terms of S, P, and D waves including helcity 0 and ±1 components as

$$\begin{aligned} d\Gamma(m_{\pi\pi}, \cos\theta_{\pi\pi}) &= 2\pi \lvert \mathcal{A}_{S_0} Y_0^0(\cos\theta_{\pi\pi}) + \mathcal{A}_{P_0} e^{i\phi_{P_0}} Y_1^0(\cos\theta_{\pi\pi}) \\ &\quad + \mathcal{A}_{D_0} e^{i\phi_{D_0}} Y_2^0(\cos\theta_{\pi\pi})\rvert^2 \\ &\quad + 2\pi \left\lvert \mathcal{A}_{P_{\pm1}} e^{i\phi_{P_{\pm1}}} \sqrt{\frac{3}{8\pi}} \sin\theta_{\pi\pi} \right. \\ &\quad \left. + \mathcal{A}_{D_{\pm1}} e^{i\phi_{D_{\pm1}}} \sqrt{\frac{15}{8\pi}} \sin\theta_{\pi\pi} \cos\theta_{\pi\pi} \right\rvert^2, \end{aligned} \quad (27)$$

where $\mathcal{A}_{k_\lambda}$ and ϕ_{k_λ} are real-valued functions of $m_{\pi\pi}$, and we have factored out the S-wave phase. We then calculate the angular moments

$$\begin{aligned} \sqrt{4\pi}\langle Y_0^0\rangle &= \mathcal{A}_{S_0}^2 + \mathcal{A}_{P_0}^2 + \mathcal{A}_{D_0}^2 + \mathcal{A}_{P_{\pm1}}^2 + \mathcal{A}_{D_{\pm1}}^2, \\ \sqrt{4\pi}\langle Y_1^0\rangle &= 2\mathcal{A}_{S_0}\mathcal{A}_{P_0}\cos\phi_{P_0} \\ &\quad + \frac{4}{\sqrt{5}}\mathcal{A}_{P_0}\mathcal{A}_{D_0}\cos(\phi_{P_0} - \phi_{D_0}) \\ &\quad + 8\sqrt{\frac{3}{5}}\mathcal{A}_{P_{\pm1}}\mathcal{A}_{D_{\pm1}}\cos(\phi_{P_{\pm1}} - \phi_{D_{\pm1}}), \\ \sqrt{4\pi}\langle Y_2^0\rangle &= \frac{2}{\sqrt{5}}\mathcal{A}_{P_0}^2 + 2\mathcal{A}_{S_0}\mathcal{A}_{D_0}\cos\phi_{D_0} \\ &\quad + \frac{2\sqrt{5}}{7}\mathcal{A}_{D_0}^2 - \frac{1}{\sqrt{5}}\mathcal{A}_{P_{\pm1}}^2 + \frac{\sqrt{5}}{7}\mathcal{A}_{D_{\pm1}}^2, \\ \sqrt{4\pi}\langle Y_3^0\rangle &= 6\sqrt{\frac{3}{35}}\mathcal{A}_{P_0}\mathcal{A}_{D_0}\cos(\phi_{P_0} - \phi_{D_0}) \\ &\quad + \frac{6}{\sqrt{35}}\mathcal{A}_{P_{\pm1}}\mathcal{A}_{D_{\pm1}}\cos(\phi_{P_{\pm1}} - \phi_{D_{\pm1}}), \\ \sqrt{4\pi}\langle Y_4^0\rangle &= \frac{6}{7}\mathcal{A}_{D_0}^2 - \frac{4}{7}\mathcal{A}_{D_{\pm1}}^2. \end{aligned} \quad (28)$$

Figure 17 shows the distributions of the angular moments for the preferred solution. In general the interpretation of these moments is that $\langle Y_0^0\rangle$ is the efficiency corrected and background subtracted event distribution; $\langle Y_1^0\rangle$ the interference of the sum of S-wave and P-wave and P-wave and D-wave amplitudes; $\langle Y_2^0\rangle$ the sum of the P-wave, D-wave, and the interference of S-wave and D-wave amplitudes; $\langle Y_3^0\rangle$ the interference between P wave and D wave; and $\langle Y_4^0\rangle$ the D wave.

In our data the $\langle Y_1^0\rangle$ distribution is consistent with zero, confirming the absence of any P wave. We do observe the effects of the $f_2(1270)$ in the $\langle Y_2^0\rangle$ distribution including the interferences with the S waves. The other moments are consistent with the absence of any structure, as expected.

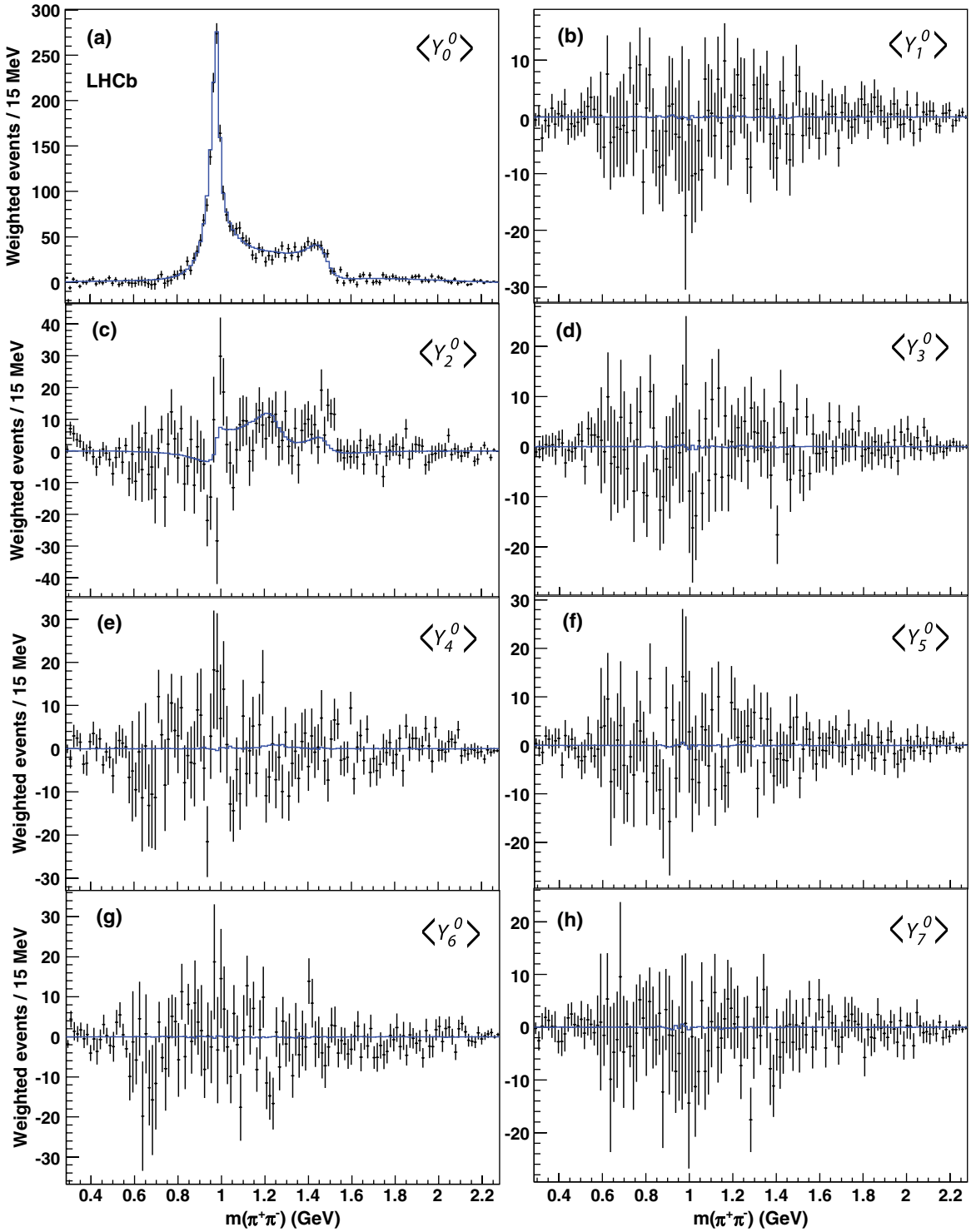

FIG. 17 (color online). The $\pi^+\pi^-$ mass dependence of the spherical harmonic moments of $\cos\theta_{\pi\pi}$ after efficiency corrections and background subtraction: (a) $\langle Y_0^0 \rangle$, (b) $\langle Y_1^0 \rangle$, (c) $\langle Y_2^0 \rangle$, (d) $\langle Y_3^0 \rangle$, (e) $\langle Y_4^0 \rangle$, (f) $\langle Y_5^0 \rangle$, (g) $\langle Y_6^0 \rangle$, and (h) $\langle Y_7^0 \rangle$. The points with error bars are the data points and the solid curves are derived from the 3R + NR preferred model.

VI. RESULTS

1. *CP* content

The main result in this paper is that *CP*-odd final states dominate. The $f_2(1270)$ helicity ± 1 yield is $(0.21 \pm 0.65)\%$. As this represents a mixed *CP* state, the upper limit on the *CP*-even fraction due to this state is $<1.3\%$ at 95% confidence level (C.L.). Adding the $\rho(770)$ amplitude and repeating the fit shows that only an insignificant amount of $\rho(770)$ can be tolerated; in fact, the

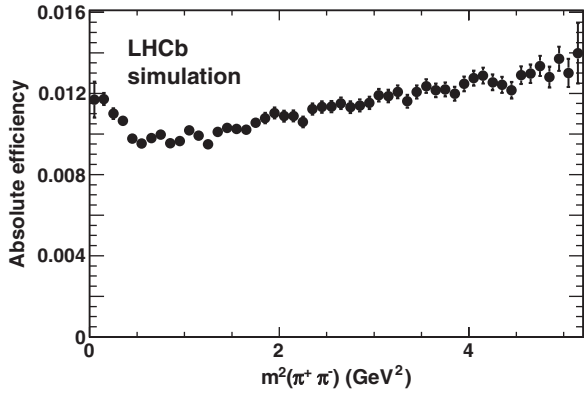

FIG. 18. Detection efficiency of $\bar{B}_s^0 \to J/\psi\pi^+\pi^-$ as a function of $s_{23} \equiv m^2(\pi^+\pi^-)$.

isospin violating $J/\psi\rho(770)$ final state is limited to $<1.5\%$ at 95% C.L. The sum of $f_2(1270)$ helicity ± 1 and $\rho(770)$ is limited to $<2.3\%$ at 95% C.L. In the $\pi^+\pi^-$ mass region within ± 90 MeV of 980 MeV, this limit improves to $<0.6\%$ at 95% C.L.

B. Total branching fraction ratio

To avoid the uncertainties associated with absolute branching fraction measurements, we quote branching fractions relative to the $\bar{B}_s^0 \to J/\psi\phi$ channel. The detection efficiency for this channel from Monte Carlo simulation is $(1.15 \pm 0.01)\%$, where the error is due to the limited Monte Carlo sample size.

The simulated detection efficiency for $\bar{B}_s^0 \to J/\psi\pi^+\pi^-$ as a function of the $m^2(\pi^+\pi^-)$ is shown in Fig. 18. The simulation does not model the pion and kaon identification efficiencies with sufficient accuracy for our purposes. Therefore, we measure the kaon identification efficiency with respect to the Monte Carlo simulation. We use samples of $D^{*+} \to \pi^+ D^0$, $D^0 \to K^-\pi^+$ events selected without kaon identification to measure the kaon and pion efficiencies with respect to the simulation, and an additional sample of $K_s^0 \to \pi^+\pi^-$ decay for pions. The identification efficiency is measured in bins of p_T and η and then the averages are weighted using the event distributions in the data. We find the correction to the $J/\psi\phi$ efficiency is 0.970 (two kaons) and that to the $J/\psi f_0$ efficiency is 0.973 (two pions). The additional correction due to particle identification then is 0.997 ± 0.010. In addition, we reweight the $\bar{B}_s^0$, p, and p_T distributions in the simulation, which lowers the $\pi^+\pi^-$ efficiency by 1.01% with respect to the K^+K^- efficiency.

Dividing the number of the $J/\psi\pi^+\pi^-$ signal events by the $J/\psi K^+K^-$ yield, applying the additional corrections as described above, and taking into account $\mathcal{B}(\phi \to K^+K^-) = (48.9 \pm 0.5)\%$ [8], we find

$$\frac{\mathcal{B}(\bar{B}_s^0 \to J/\psi\pi^+\pi^-)}{\mathcal{B}(\bar{B}_s^0 \to J/\psi\phi)} = (19.79 \pm 0.47 \pm 0.52)\%.$$

Whenever two uncertainties are quoted, the first is statistical and the second systematic. The latter will be discussed later in Sec. VII. This branching fraction ratio has not been previously measured.

C. Relative resonance yields

Next we evaluate the relative yields for the 3R + NR fit to the $J/\psi\pi^+\pi^-$ final state from the preferred solution. We normalize the individual fit fractions reported in Table V by the sum. These normalized fit fractions are listed in Table IX along with the branching fraction relative to $J/\psi\phi$, defined as R_r, where r refers to the particular final state under consideration. Thus

$$R_r = \frac{\mathcal{B}(\bar{B}_s^0 \to r)}{\mathcal{B}(\bar{B}_s^0 \to J/\psi\phi)}. \tag{29}$$

We use the difference between the preferred and alternate solutions found for the 3R + NR fit to assign a systematic uncertainty. Other systematic uncertainties are described in Sec. VII.

The value found for R_r for the $f_0(980)$, $0.139 \pm 0.006^{+0.025}_{-0.012}$, is consistent with the prediction of Ref. [9] and consistent with the our first observation using 33 pb^{-1} of integrated luminosity [1], after multiplying by $\mathcal{B}(\phi \to K^+K^-)$. The decay $\bar{B}_s^0 \to J/\psi f_0(1370)$ is now established. Previously both LHCb [1] and Belle [2] had seen evidence for this final state. The normalized $f_2(1270)$ helicity zero rate is $(0.49 \pm 0.16)\%$ in the preferred model and $(0.42 \pm 0.11)\%$ for the alternate solution.

TABLE IX. Normalized fit fractions (%) for alternate and preferred 3R + NR models and the ratio R (%) relative to $\bar{B}_s^0 \to J/\psi\phi$. The numbers for the $f_2(1270)$ refer only to the $\lambda = 0$ state.

State	Preferred	Alternate	R preferred	R alternate	Final R
$f_0(980)$	69.7 ± 2.3	82.4 ± 2.3	13.9 ± 0.6	16.3 ± 0.6	$13.9 \pm 0.6^{+2.5}_{-1.2}$
$f_0(1370)$	21.2 ± 2.7	5.7 ± 0.7	4.19 ± 0.53	1.13 ± 0.15	$4.19 \pm 0.53^{+0.12}_{-3.70}$
NR	8.4 ± 1.5	11.3 ± 1.9	1.66 ± 0.31	2.23 ± 0.39	$1.66 \pm 0.31^{+0.96}_{-0.08}$
$f_2(1270)$	0.49 ± 0.16	0.42 ± 0.11	0.098 ± 0.033	0.083 ± 0.022	$0.098 \pm 0.033^{+0.006}_{-0.015}$

TABLE X. Relative systematic uncertainties on R (%).

Parameter	Total	$f_0(980)$	$f_0(1370)$	NR	$f_2(1270)$, $\lambda = 0$
$m(\pi^+\pi^-)$-dependent efficiency	1.0	0.2	0.2	1.0	0.2
PID efficiency	2.0	2.0	2.0	2.0	2.0
$J/\psi\phi$ S wave	0.7	0.7	0.7	0.7	0.7
$\bar{B}_s^0$ p and p_T distributions	0.5	0.5	0.5	0.5	0.5
Acceptance function	0	0.1	1.3	1.4	3.9
$\mathcal{B}(\phi \to K^+K^-)$	1.0	1.0	1.0	1.0	1.0
Background	0.6	0.6	0.6	0.6	0.6
Resonance fit	...	$^{+18.2}_{-8.0}$	$^{+0.8}_{-88.1}$	$^{+57.6}_{-3.7}$	$^{+3.0}_{-15.8}$
Total	± 2.7	$^{+18.3}_{-8.4}$	$^{+2.9}_{-88.2}$	$^{+57.7}_{-4.8}$	$^{+5.5}_{-16.4}$

VII. SYSTEMATIC UNCERTAINTIES

Systematic uncertainties on the CP-odd fraction are negligible. In fact, using any of the alternate fits with different additional components does not introduce any significant fractions of CP-odd final states.

The systematic uncertainties on the branching fraction ratios have several contributions listed in Table X. Since R_r is measured relative to $J/\psi\phi$ there is no systematic uncertainty due to differences in the tracking performance between data and simulation. The $J/\psi\phi$ P-wave yield is fully correlated with the S-wave yield whose uncertainty we estimate as 0.7% by changing the signal PDF and the background shape. By far the largest uncertainty in every rate, except the total, is caused by our choice of the preferred versus the alternate solutions. Using the difference between these fit results for the systematic uncertainty causes relatively large and asymmetric values. We also include systematic uncertainties due to the possible presence of the $\rho(770)$, the $f_0(1500)$, or the $f_0(600)$ resonances by taking the maximum difference between the fit including one of these resonances and our preferred solution, if the difference is larger than the one between the preferred and alternate 3R + NR fit. In the case of the $f_0(1500)$ the preferred solution is pathological in that it produces an unacceptably large $f_0(1370)$ component along with a 214% component sum; therefore, here we use the alternate solution that is much better behaved.

The uncertainty from the Monte Carlo sample size for the mass-dependent $\pi^+\pi^-$ efficiencies are accounted for in the statistical errors; a residual systematic uncertainty is included that results from allowed changes in the shape due to the distribution of the events. The size of these differences depends on the mass range for the particular component multiplied by the possible efficiency variation across this mass range. This is estimated as 1% for the entire mass range and is smaller for individual resonances. Small uncertainties are introduced if the simulation does not have the correct $\bar{B}_s^0$ kinematic distributions. We are relatively insensitive to any of these differences in the $\bar{B}_s^0$, p, and p_T distributions since we are measuring relative rates. These distributions are varied by changing the weights in each bin by plus and minus the statistical error in that bin. We see at most a 0.5% change. There is a 2% systematic uncertainty assigned for the relative particle identification efficiencies. These efficiencies have been corrected from those predicted in the simulation by using pion data from $K_s^0 \to \pi^+\pi^-$ decays and kaon and pion

TABLE XI. Changes due to modified acceptance function.

Values	Original	After change	Variation (%)
Fit fractions			
$f_0(980)$	$(107.1 \pm 3.5)\%$	107.2%	0.1
$f_2(1270)$ $\lambda = 0$	$(0.76 \pm 0.25)\%$	0.79%	3.9
$f_2(1270)$ $\lvert\lambda\rvert = 1$	$(0.33 \pm 1.00)\%$	0.26%	21.2
$f_0(1370)$	$(32.6 \pm 4.1)\%$	31.2%	1.3
NR	$(12.8 \pm 2.3)\%$	12.7%	1.4
$f_0(980)$ parameters			
m_{f_0}(MeV)	939.9 ± 6.3	938.4	0.16
$g_{\pi\pi}$(MeV)	199 ± 30	205	2.7
$g_{KK}/g_{\pi\pi}$	3.01 ± 0.25	3.05	1.3
$f_0(1370)$ parameters			
m_{f_0}(MeV)	1475.1 ± 6.3	1476.4	0.09
Γ(MeV)	112.7 ± 11.1	113.0	0.27

data from $D^{*\pm} \to \pi^{\pm} D^0(\bar{D}^0)$, $D^0(\bar{D}^0) \to K^{\mp}\pi^{\pm}$ decays. The uncertainty on the corrections is 0.5% per track. The background modeling was changed by using a second-order polynomial shape in the $J/\psi\pi^+\pi^-$ mass fit giving a 0.6% change in the signal yield. Since the input $f_0(1370)$ mass and width parameters were allowed to vary within Gaussian constraints, there is no additional uncertainty to account for.

The effect on the fit fractions of changing the acceptance function is also evaluated. Since the acceptance model was tested by its agreement with the $\bar{B}^0_s \to J/\psi K^+K^-$ data in Fig. 9, we vary the data so that the model does not fit as well. This is accomplished by increasing the minimum IP χ^2 requirement from 9 to 12.25 on both of the kaon candidates, which has the effect of increasing the χ^2/ndf of the fit to angular distributions by 1 unit. The Monte Carlo simulation of $\bar{B}^0_s \to J/\psi\pi^+\pi^-$ with the changed requirement is then fitted to get an acceptance function. This acceptance function is then applied to the data with the original minimum IP χ^2 cut of 9, and the likelihood fit is redone. The resulting fitted values from the preferred solution are compared with the original values in Table XI. The changes are small and well within the statistical uncertainties.

VIII. CONCLUSIONS

We have studied the resonance structure of $\bar{B}^0_s \to J/\psi\pi^+\pi^-$ using a modified Dalitz plot analysis where we also include the decay angle of the J/ψ. The decay distributions are formed from a series of final states described by individual $\pi^+\pi^-$ interfering decay amplitudes. The largest component is the $f_0(980)$ that is described by a Flatté function. The data are best described by adding Breit-Wigner amplitudes for the $f_0(1370)$, the $f_2(1270)$ resonances, and a nonresonance contribution. Adding a $\rho(770)$ into the fit does not improve the overall likelihood. Inclusion of $f_0(600)$ or $f_0(1500)$ does not result in significant signals for these resonances.

Our three resonance plus nonresonance best fit is dominantly a CP-odd S wave over the entire signal region. We also have a D-wave component arising from the $f_2(1270)$ resonance. Part of this corresponds to the A_{20} amplitude that is also pure CP-odd and is $(0.49 \pm 0.16^{+0.02}_{-0.08})\%$ of the total rate. A mixed CP part corresponding to the $A_{2\pm1}$ amplitude is $(0.2 \pm 0.7)\%$ of the total. Adding this to the amount of allowed $\rho(770)$, less than 1.5% at 95% C.L., we find that the CP-odd fraction is greater than 0.977 at 95% C.L. Thus, the entire mass range can be used to study CP violation with this almost pure CP-odd final state.

The measured relative branching ratio is

$$\frac{\mathcal{B}(\bar{B}^0_s \to J/\psi\pi^+\pi^-)}{\mathcal{B}(\bar{B}^0_s \to J/\psi\phi)} = (19.79 \pm 0.47 \pm 0.52)\%,$$

where the first uncertainty is statistical and the second systematic. The largest component is the $f_0(980)$ resonance. We also determine

$$\frac{\mathcal{B}(\bar{B}^0_s \to J/\psi\pi^+\pi^-)\mathcal{B}(f_0(980) \to \pi^+\pi^-)}{\mathcal{B}(\bar{B}^0_s \to J/\psi\phi)} = (13.9 \pm 0.6^{+2.5}_{-1.2})\%.$$

This state was predicted to exist and have a branching fraction about 10% that of $J/\psi\phi$ [9]. Our new measurement is consistent with and somewhat larger than this prediction. Other models give somewhat higher rates [25]. We also have firmly established the existence of the $J/\psi f_0(1370)$ final state in $\bar{B}^0_s$ decay.

ACKNOWLEDGMENTS

We express our gratitude to our colleagues in the CERN accelerator departments for the excellent performance of the LHC. We thank the technical and administrative staff at CERN and at the LHCb institutes, and acknowledge support from the National Agencies: CAPES, CNPq, FAPERJ, and FINEP (Brazil); CERN; NSFC (China); CNRS/IN2P3 (France); BMBF, DFG, HGF, and MPG (Germany); SFI (Ireland); INFN (Italy); FOM and NWO (Netherlands); SCSR (Poland); ANCS (Romania); MinES of Russia and Rosatom (Russia); MICINN, XuntaGal and GENCAT (Spain); SNSF and SER (Switzerland); NAS Ukraine (Ukraine); STFC (United Kingdom); NSF (USA). We also acknowledge the support received from the ERC under FP7 and the Region Auvergne.

[1] R. Aaij *et al.* (LHCb Collaboration), Phys. Lett. B **698**, 115 (2011).
[2] J. Li *et al.* (Belle Collaboration), Phys. Rev. Lett. **106**, 121802 (2011); V. M. Abazov *et al.* (D0 Collaboration), Phys. Rev. D **85**, 011103 (2012); T. Aaltonen *et al.* (CDF Collaboration), Phys. Rev. D **84**, 052012 (2011).
[3] R. Aaij *et al.* (LHCb Collaboration), Phys. Lett. B **707**, 497 (2012).
[4] R. Aaij *et al.* (LHCb Collaboration), Phys. Rev. Lett. **108**, 101803 (2012).
[5] T. Aaltonen *et al.* (CDF Collaboration), Phys. Rev. D **85**, 072002 (2012); V. M. Abazov *et al.* (D0 Collaboration), Phys. Rev. D **85**, 032006 (2012).
[6] R. Dalitz, Philos. Mag. **44**, 1068 (1953).
[7] A. Alves, Jr. *et al.* (LHCb Collaboration), JINST **3**, S08005 (2008).

[8] K. Nakamura *et al.* (Particle Data Group), J. Phys. G **37**, 075021 (2010).
[9] S. Stone and L. Zhang, Phys. Rev. D **79**, 074024 (2009).
[10] M. Pivk and F. R. Le Diberder, Nucl. Instrum. Methods Phys. Res., Sect. A **555**, 356 (2005).
[11] R. Mizuk *et al.* (Belle Collaboration), Phys. Rev. D **78**, 072004 (2008).
[12] R. Mizuk *et al.* (Belle Collaboration), Phys. Rev. D **80**, 031104 (2009).
[13] J. M. Blatt and V. F. Weisskopf, *Theoretical Nuclear Physics* (Wiley, New York, 1952).
[14] S. M. Flatté, Phys. Lett. **63B**, 228 (1976).
[15] T. Sjöstrand, S. Mrenna, and P. Skands, J. High Energy Phys. 05 (2006) 026.
[16] I. Belyaev *et al.*, *Handling of the Generation of Primary Events in Gauss, the LHCb Simulation Framework* (Nuclear Science Symposium Conference Record (NSS/MIC) IEEE, 2010), p. 1155.
[17] S. Agostinelli *et al.* (GEANT4 Collaboration), Nucl. Instrum. Methods Phys. Res., Sect. A **506**, 250 (2003).
[18] M. Clemencic *et al.*, J. Phys. Conf. Ser. **331**, 032023 (2011).
[19] J. Allison, Comput. Phys. Commun. **77**, 377 (1993).
[20] H. Muramatsu *et al.* (CLEO Collaboration), Phys. Rev. Lett. **89**, 251802 (2002).
[21] E. M. Aitala *et al.* (E791 Collaboration), Phys. Rev. Lett. **86**, 765 (2001).
[22] S. Baker and R. D. Cousins, Nucl. Instrum. Methods Phys. Res., Sect. A **221**, 437 (1984).
[23] M. Ablikim *et al.* (BES Collaboration), Phys. Lett. B **607**, 243 (2005).
[24] J. Lees (*BABAR* Collaboration), Phys. Rev. D **85**, 112010 (2012); P. del Amo Sanchez *et al.* (*BABAR* Collaboration), Phys. Rev. D **83**, 052001 (2011).
[25] P. Colangelo, F. De Fazio, and W. Wang, Phys. Rev. D **83**, 094027 (2011); **81**, 074001 (2010); R. Fleischer, R. Knegjens, and G. Ricciardi, Eur. Phys. J. C **71**, 1832 (2011); B. El-Bennich, J. de Melo, O. Leitner, B. Loiseau, and J. Dedonder, Prog. Part. Nucl. Phys. **67**, 395 (2012); O. Leitner, J.-P. Dedonder, B. Loiseau, and B. El-Bennich, Phys. Rev. D **82**, 076006 (2010).

R. Aaij,[38] C. Abellan Beteta,[33,a] B. Adeva,[34] M. Adinolfi,[43] C. Adrover,[6] A. Affolder,[49] Z. Ajaltouni,[5] J. Albrecht,[35] F. Alessio,[35] M. Alexander,[48] S. Ali,[38] G. Alkhazov,[27] P. Alvarez Cartelle,[34] A. A. Alves Jr,[22] S. Amato,[2] Y. Amhis,[36] J. Anderson,[37] R. B. Appleby,[51] O. Aquines Gutierrez,[10] F. Archilli,[18,35] A. Artamonov,[32] M. Artuso,[53,35] E. Aslanides,[6] G. Auriemma,[22,b] S. Bachmann,[11] J. J. Back,[45] V. Balagura,[28,35] W. Baldini,[16] R. J. Barlow,[51] C. Barschel,[35] S. Barsuk,[7] W. Barter,[44] A. Bates,[48] C. Bauer,[10] Th. Bauer,[38] A. Bay,[36] I. Bediaga,[1] S. Belogurov,[28] K. Belous,[32] I. Belyaev,[28] E. Ben-Haim,[8] M. Benayoun,[8] G. Bencivenni,[18] S. Benson,[47] J. Benton,[43] R. Bernet,[37] M.-O. Bettler,[17] M. van Beuzekom,[38] A. Bien,[11] S. Bifani,[12] T. Bird,[51] A. Bizzeti,[17,c] P. M. Bjørnstad,[51] T. Blake,[35] F. Blanc,[36] C. Blanks,[50] J. Blouw,[11] S. Blusk,[53] A. Bobrov,[31] V. Bocci,[22] A. Bondar,[31] N. Bondar,[27] W. Bonivento,[15] S. Borghi,[48,51] A. Borgia,[53] T. J. V. Bowcock,[49] C. Bozzi,[16] T. Brambach,[9] J. van den Brand,[39] J. Bressieux,[36] D. Brett,[51] M. Britsch,[10] T. Britton,[53] N. H. Brook,[43] H. Brown,[49] A. Büchler-Germann,[37] I. Burducea,[26] A. Bursche,[37] J. Buytaert,[35] S. Cadeddu,[15] O. Callot,[7] M. Calvi,[20,d] M. Calvo Gomez,[33,a] A. Camboni,[33] P. Campana,[18,35] A. Carbone,[14] G. Carboni,[21,e] R. Cardinale,[19,35,f] A. Cardini,[15] L. Carson,[50] K. Carvalho Akiba,[2] G. Casse,[49] M. Cattaneo,[35] Ch. Cauet,[9] M. Charles,[52] Ph. Charpentier,[35] N. Chiapolini,[37] K. Ciba,[35] X. Cid Vidal,[34] G. Ciezarek,[50] P. E. L. Clarke,[47] M. Clemencic,[35] H. V. Cliff,[44] J. Closier,[35] C. Coca,[26] V. Coco,[38] J. Cogan,[6] P. Collins,[35] A. Comerma-Montells,[33] A. Contu,[52] A. Cook,[43] M. Coombes,[43] G. Corti,[35] B. Couturier,[35] G. A. Cowan,[36] R. Currie,[47] C. D'Ambrosio,[35] P. David,[8] P. N. Y. David,[38] I. De Bonis,[4] K. De Bruyn,[38] S. De Capua,[21,e] M. De Cian,[37] J. M. De Miranda,[1] L. De Paula,[2] P. De Simone,[18] D. Decamp,[4] M. Deckenhoff,[9] H. Degaudenzi,[36,35] L. Del Buono,[8] C. Deplano,[15] D. Derkach,[14,35] O. Deschamps,[5] F. Dettori,[39] J. Dickens,[44] H. Dijkstra,[35] P. Diniz Batista,[1] F. Domingo Bonal,[33,a] S. Donleavy,[49] F. Dordei,[11] A. Dosil Suárez,[34] D. Dossett,[45] A. Dovbnya,[40] F. Dupertuis,[36] R. Dzhelyadin,[32] A. Dziurda,[23] S. Easo,[46] U. Egede,[50] V. Egorychev,[28] S. Eidelman,[31] D. van Eijk,[38] F. Eisele,[11] S. Eisenhardt,[47] R. Ekelhof,[9] L. Eklund,[48] Ch. Elsasser,[37] D. Elsby,[42] D. Esperante Pereira,[34] A. Falabella,[16,14,g] C. Färber,[11] G. Fardell,[47] C. Farinelli,[38] S. Farry,[12] V. Fave,[36] V. Fernandez Albor,[34] M. Ferro-Luzzi,[35] S. Filippov,[30] C. Fitzpatrick,[47] M. Fontana,[10] F. Fontanelli,[19,f] R. Forty,[35] O. Francisco,[2] M. Frank,[35] C. Frei,[35] M. Frosini,[17,h] S. Furcas,[20] A. Gallas Torreira,[34] D. Galli,[14,i] M. Gandelman,[2] P. Gandini,[52] Y. Gao,[3] J-C. Garnier,[35] J. Garofoli,[53] J. Garra Tico,[44] L. Garrido,[33] D. Gascon,[33] C. Gaspar,[35] R. Gauld,[52] N. Gauvin,[36] M. Gersabeck,[35] T. Gershon,[45,35] Ph. Ghez,[4] V. Gibson,[44] V. V. Gligorov,[35] C. Göbel,[54] D. Golubkov,[28] A. Golutvin,[50,28,35] A. Gomes,[2] H. Gordon,[52] M. Grabalosa Gándara,[33] R. Graciani Diaz,[33] L. A. Granado Cardoso,[35] E. Graugés,[33] G. Graziani,[17] A. Grecu,[26] E. Greening,[52] S. Gregson,[44] B. Gui,[53] E. Gushchin,[30] Yu. Guz,[32] T. Gys,[35] C. Hadjivasiliou,[53] G. Haefeli,[36] C. Haen,[35] S. C. Haines,[44] T. Hampson,[43] S. Hansmann-Menzemer,[11] R. Harji,[50] N. Harnew,[52] J. Harrison,[51] P. F. Harrison,[45] T. Hartmann,[55] J. He,[7] V. Heijne,[38] K. Hennessy,[49] P. Henrard,[5] J. A. Hernando Morata,[34] E. van Herwijnen,[35] E. Hicks,[49] K. Holubyev,[11] P. Hopchev,[4] W. Hulsbergen,[38] P. Hunt,[52] T. Huse,[49] R. S. Huston,[12] D. Hutchcroft,[49] D. Hynds,[48] V. Iakovenko,[41]

P. Ilten,[12] J. Imong,[43] R. Jacobsson,[35] A. Jaeger,[11] M. Jahjah Hussein,[5] E. Jans,[38] F. Jansen,[38] P. Jaton,[36] B. Jean-Marie,[7] F. Jing,[3] M. John,[52] D. Johnson,[52] C. R. Jones,[44] B. Jost,[35] M. Kaballo,[9] S. Kandybei,[40] M. Karacson,[35] T. M. Karbach,[9] J. Keaveney,[12] I. R. Kenyon,[42] U. Kerzel,[35] T. Ketel,[39] A. Keune,[36] B. Khanji,[6] Y. M. Kim,[47] M. Knecht,[36] R. F. Koopman,[39] P. Koppenburg,[38] M. Korolev,[29] A. Kozlinskiy,[38] L. Kravchuk,[30] K. Kreplin,[11] M. Kreps,[45] G. Krocker,[11] P. Krokovny,[31] F. Kruse,[9] K. Kruzelecki,[35] M. Kucharczyk,[20,23,35,d] V. Kudryavtsev,[31] T. Kvaratskheliya,[28,35] V. N. La Thi,[36] D. Lacarrere,[35] G. Lafferty,[51] A. Lai,[15] D. Lambert,[47] R. W. Lambert,[39] E. Lanciotti,[35] G. Lanfranchi,[18] C. Langenbruch,[35] T. Latham,[45] C. Lazzeroni,[42] R. Le Gac,[6] J. van Leerdam,[38] J.-P. Lees,[4] R. Lefèvre,[5] A. Leflat,[29,35] J. Lefrançois,[7] O. Leroy,[6] T. Lesiak,[23] L. Li,[3] L. Li Gioi,[5] M. Lieng,[9] M. Liles,[49] R. Lindner,[35] C. Linn,[11] B. Liu,[3] G. Liu,[35] J. von Loeben,[20] J. H. Lopes,[2] E. Lopez Asamar,[33] N. Lopez-March,[36] H. Lu,[3] J. Luisier,[36] A. Mac Raighne,[48] F. Machefert,[7] I. V. Machikhiliyan,[4,28] F. Maciuc,[10] O. Maev,[27,35] J. Magnin,[1] S. Malde,[52] R. M. D. Mamunur,[35] G. Manca,[15,j] G. Mancinelli,[6] N. Mangiafave,[44] U. Marconi,[14] R. Märki,[36] J. Marks,[11] G. Martellotti,[22] A. Martens,[8] L. Martin,[52] A. Martín Sánchez,[7] M. Martinelli,[38] D. Martinez Santos,[35] A. Massafferri,[1] Z. Mathe,[12] C. Matteuzzi,[20] M. Matveev,[27] E. Maurice,[6] B. Maynard,[53] A. Mazurov,[16,30,35] G. McGregor,[51] R. McNulty,[12] M. Meissner,[11] M. Merk,[38] J. Merkel,[9] S. Miglioranzi,[35] D. A. Milanes,[13] M.-N. Minard,[4] J. Molina Rodriguez,[54] S. Monteil,[5] D. Moran,[12] P. Morawski,[23] R. Mountain,[53] I. Mous,[38] F. Muheim,[47] K. Müller,[37] R. Muresan,[26] B. Muryn,[24] B. Muster,[36] J. Mylroie-Smith,[49] P. Naik,[43] T. Nakada,[36] R. Nandakumar,[46] I. Nasteva,[1] M. Needham,[47] N. Neufeld,[35] A. D. Nguyen,[36] C. Nguyen-Mau,[36,k] M. Nicol,[7] V. Niess,[5] N. Nikitin,[29] T. Nikodem,[11] A. Nomerotski,[52,35] A. Novoselov,[32] A. Oblakowska-Mucha,[24] V. Obraztsov,[32] S. Oggero,[38] S. Ogilvy,[48] O. Okhrimenko,[41] R. Oldeman,[15,35,j] M. Orlandea,[26] J. M. Otalora Goicochea,[2] P. Owen,[50] B. K. Pal,[53] J. Palacios,[37] A. Palano,[13,l] M. Palutan,[18] J. Panman,[35] A. Papanestis,[46] M. Pappagallo,[48] C. Parkes,[51] C. J. Parkinson,[50] G. Passaleva,[17] G. D. Patel,[49] M. Patel,[50] S. K. Paterson,[50] G. N. Patrick,[46] C. Patrignani,[19,f] C. Pavel-Nicorescu,[26] A. Pazos Alvarez,[34] A. Pellegrino,[38] G. Penso,[22,m] M. Pepe Altarelli,[35] S. Perazzini,[14,i] D. L. Perego,[20,d] E. Perez Trigo,[34] A. Pérez-Calero Yzquierdo,[33] P. Perret,[5] M. Perrin-Terrin,[6] G. Pessina,[20] A. Petrolini,[19,f] A. Phan,[53] E. Picatoste Olloqui,[33] B. Pie Valls,[33] B. Pietrzyk,[4] T. Pilař,[45] D. Pinci,[22] R. Plackett,[48] S. Playfer,[47] M. Plo Casasus,[34] G. Polok,[23] A. Poluektov,[45,31] E. Polycarpo,[2] D. Popov,[10] B. Popovici,[26] C. Potterat,[33] A. Powell,[52] J. Prisciandaro,[36] V. Pugatch,[41] A. Puig Navarro,[33] W. Qian,[53] J. H. Rademacker,[43] B. Rakotomiaramanana,[36] M. S. Rangel,[2] I. Raniuk,[40] G. Raven,[39] S. Redford,[52] M. M. Reid,[45] A. C. dos Reis,[1] S. Ricciardi,[46] A. Richards,[50] K. Rinnert,[49] D. A. Roa Romero,[5] P. Robbe,[7] E. Rodrigues,[48,51] F. Rodrigues,[2] P. Rodriguez Perez,[34] G. J. Rogers,[44] S. Roiser,[35] V. Romanovsky,[32] M. Rosello,[33,a] J. Rouvinet,[36] T. Ruf,[35] H. Ruiz,[33] G. Sabatino,[21,e] J. J. Saborido Silva,[34] N. Sagidova,[27] P. Sail,[48] B. Saitta,[15,j] C. Salzmann,[37] M. Sannino,[19,f] R. Santacesaria,[22] C. Santamarina Rios,[34] R. Santinelli,[35] E. Santovetti,[21,e] M. Sapunov,[6] A. Sarti,[18,m] C. Satriano,[22,b] A. Satta,[21] M. Savrie,[16,g] D. Savrina,[28] P. Schaack,[50] M. Schiller,[39] H. Schindler,[35] S. Schleich,[9] M. Schlupp,[9] M. Schmelling,[10] B. Schmidt,[35] O. Schneider,[36] A. Schopper,[35] M.-H. Schune,[7] R. Schwemmer,[35] B. Sciascia,[18] A. Sciubba,[18,m] M. Seco,[34] A. Semennikov,[28] K. Senderowska,[24] I. Sepp,[50] N. Serra,[37] J. Serrano,[6] P. Seyfert,[11] M. Shapkin,[32] I. Shapoval,[40,35] P. Shatalov,[28] Y. Shcheglov,[27] T. Shears,[49] L. Shekhtman,[31] O. Shevchenko,[40] V. Shevchenko,[28] A. Shires,[50] R. Silva Coutinho,[45] T. Skwarnicki,[53] N. A. Smith,[49] E. Smith,[52,46] K. Sobczak,[5] F. J. P. Soler,[48] A. Solomin,[43] F. Soomro,[18,35] B. Souza De Paula,[2] B. Spaan,[9] A. Sparkes,[47] P. Spradlin,[48] F. Stagni,[35] S. Stahl,[11] O. Steinkamp,[37] S. Stoica,[26] S. Stone,[53,35] B. Storaci,[38] M. Straticiuc,[26] U. Straumann,[37] V. K. Subbiah,[35] S. Swientek,[9] M. Szczekowski,[25] P. Szczypka,[36] T. Szumlak,[24] S. T'Jampens,[4] E. Teodorescu,[26] F. Teubert,[35] C. Thomas,[52] E. Thomas,[35] J. van Tilburg,[11] V. Tisserand,[4] M. Tobin,[37] S. Tolk,[39] S. Topp-Joergensen,[52] N. Torr,[52] E. Tournefier,[4,50] S. Tourneur,[36] M. T. Tran,[36] A. Tsaregorodtsev,[6] N. Tuning,[38] M. Ubeda Garcia,[35] A. Ukleja,[25] U. Uwer,[11] V. Vagnoni,[14] G. Valenti,[14] R. Vazquez Gomez,[33] P. Vazquez Regueiro,[34] S. Vecchi,[16] J. J. Velthuis,[43] M. Veltri,[17,n] B. Viaud,[7] I. Videau,[7] D. Vieira,[2] X. Vilasis-Cardona,[33,a] J. Visniakov,[34] A. Vollhardt,[37] D. Volyanskyy,[10] D. Voong,[43] A. Vorobyev,[27] V. Vorobyev,[31] H. Voss,[10] R. Waldi,[55] S. Wandernoth,[11] J. Wang,[53] D. R. Ward,[44] N. K. Watson,[42] A. D. Webber,[51] D. Websdale,[50] M. Whitehead,[45] D. Wiedner,[11] L. Wiggers,[38] G. Wilkinson,[52] M. P. Williams,[45,46] M. Williams,[50] F. F. Wilson,[46] J. Wishahi,[9] M. Witek,[23] W. Witzeling,[35] S. A. Wotton,[44] K. Wyllie,[35] Y. Xie,[47] F. Xing,[52] Z. Xing,[53] Z. Yang,[3] R. Young,[47] O. Yushchenko,[32] M. Zangoli,[14] M. Zavertyaev,[10,o] F. Zhang,[3] L. Zhang,[53] W. C. Zhang,[12] Y. Zhang,[3] A. Zhelezov,[11] L. Zhong,[3] and A. Zvyagin[35]

(LHCb Collaboration)

[1]*Centro Brasileiro de Pesquisas Físicas (CBPF), Rio de Janeiro, Brazil*
[2]*Universidade Federal do Rio de Janeiro (UFRJ), Rio de Janeiro, Brazil*
[3]*Center for High Energy Physics, Tsinghua University, Beijing, China*
[4]*LAPP, Université de Savoie, CNRS/IN2P3, Annecy-Le-Vieux, France*
[5]*Clermont Université, Université Blaise Pascal, CNRS/IN2P3, LPC, Clermont-Ferrand, France*
[6]*CPPM, Aix-Marseille Université, CNRS/IN2P3, Marseille, France*
[7]*LAL, Université Paris-Sud, CNRS/IN2P3, Orsay, France*
[8]*LPNHE, Université Pierre et Marie Curie, Université Paris Diderot, CNRS/IN2P3, Paris, France*
[9]*Fakultät Physik, Technische Universität Dortmund, Dortmund, Germany*
[10]*Max-Planck-Institut für Kernphysik (MPIK), Heidelberg, Germany*
[11]*Physikalisches Institut, Ruprecht-Karls-Universität Heidelberg, Heidelberg, Germany*
[12]*School of Physics, University College Dublin, Dublin, Ireland*
[13]*Sezione INFN di Bari, Bari, Italy*
[14]*Sezione INFN di Bologna, Bologna, Italy*
[15]*Sezione INFN di Cagliari, Cagliari, Italy*
[16]*Sezione INFN di Ferrara, Ferrara, Italy*
[17]*Sezione INFN di Firenze, Firenze, Italy*
[18]*Laboratori Nazionali dell'INFN di Frascati, Frascati, Italy*
[19]*Sezione INFN di Genova, Genova, Italy*
[20]*Sezione INFN di Milano Bicocca, Milano, Italy*
[21]*Sezione INFN di Roma Tor Vergata, Roma, Italy*
[22]*Sezione INFN di Roma La Sapienza, Roma, Italy*
[23]*Henryk Niewodniczanski Institute of Nuclear Physics Polish Academy of Sciences, Kraków, Poland*
[24]*AGH University of Science and Technology, Kraków, Poland*
[25]*Soltan Institute for Nuclear Studies, Warsaw, Poland*
[26]*Horia Hulubei National Institute of Physics and Nuclear Engineering, Bucharest-Magurele, Romania*
[27]*Petersburg Nuclear Physics Institute (PNPI), Gatchina, Russia*
[28]*Institute of Theoretical and Experimental Physics (ITEP), Moscow, Russia*
[29]*Institute of Nuclear Physics, Moscow State University (SINP MSU), Moscow, Russia*
[30]*Institute for Nuclear Research of the Russian Academy of Sciences (INR RAN), Moscow, Russia*
[31]*Budker Institute of Nuclear Physics (SB RAS) and Novosibirsk State University, Novosibirsk, Russia*
[32]*Institute for High Energy Physics (IHEP), Protvino, Russia*
[33]*Universitat de Barcelona, Barcelona, Spain*
[34]*Universidad de Santiago de Compostela, Santiago de Compostela, Spain*
[35]*European Organization for Nuclear Research (CERN), Geneva, Switzerland*
[36]*Ecole Polytechnique Fédérale de Lausanne (EPFL), Lausanne, Switzerland*
[37]*Physik-Institut, Universität Zürich, Zürich, Switzerland*
[38]*Nikhef National Institute for Subatomic Physics, Amsterdam, The Netherlands*
[39]*Nikhef National Institute for Subatomic Physics and VU University Amsterdam, Amsterdam, The Netherlands*
[40]*NSC Kharkiv Institute of Physics and Technology (NSC KIPT), Kharkiv, Ukraine*
[41]*Institute for Nuclear Research of the National Academy of Sciences (KINR), Kyiv, Ukraine*
[42]*University of Birmingham, Birmingham, United Kingdom*
[43]*H. H. Wills Physics Laboratory, University of Bristol, Bristol, United Kingdom*
[44]*Cavendish Laboratory, University of Cambridge, Cambridge, United Kingdom*
[45]*Department of Physics, University of Warwick, Coventry, United Kingdom*
[46]*STFC Rutherford Appleton Laboratory, Didcot, United Kingdom*
[47]*School of Physics and Astronomy, University of Edinburgh, Edinburgh, United Kingdom*
[48]*School of Physics and Astronomy, University of Glasgow, Glasgow, United Kingdom*
[49]*Oliver Lodge Laboratory, University of Liverpool, Liverpool, United Kingdom*
[50]*Imperial College London, London, United Kingdom*
[51]*School of Physics and Astronomy, University of Manchester, Manchester, United Kingdom*
[52]*Department of Physics, University of Oxford, Oxford, United Kingdom*
[53]*Syracuse University, Syracuse, New York, United States*
[54]*Pontifícia Universidade Católica do Rio de Janeiro (PUC-Rio), Rio de Janeiro, Brazil [associated with Universidade Federal do Rio de Janeiro (UFRJ), Rio de Janeiro, Brazil]*
[55]*Institut für Physik, Universität Rostock, Rostock, Germany (associated with Physikalisches Institut, Ruprecht-Karls-Universität Heidelberg, Heidelberg, Germany)*

[a]Also at LIFAELS, La Salle, Universitat Ramon Llull, Barcelona, Spain.
[b]Also at Università della Basilicata, Potenza, Italy.
[c]Also at Università di Modena e Reggio Emilia, Modena, Italy.
[d]Also at Università di Milano Bicocca, Milano, Italy.
[e]Also at Università di Roma Tor Vergata, Roma, Italy.
[f]Also at Università di Genova, Genova, Italy.
[g]Also at Università di Ferrara, Ferrara, Italy.
[h]Also at Università di Firenze, Firenze, Italy.
[i]Also at Università di Bologna, Bologna, Italy.
[j]Also at Università di Cagliari, Cagliari, Italy.
[k]Also at Hanoi University of Science, Hanoi, Viet Nam.
[l]Also at Università di Bari, Bari, Italy.
[m]Also at Università di Roma La Sapienza, Roma, Italy.
[n]Also at Università di Urbino, Urbino, Italy.
[o]Also at P.N. Lebedev Physical Institute, Russian Academy of Science (LPI RAS), Moscow, Russia.